Efficient starshade retargeting architecture using chemical propulsion

Thibault L. B. Flinois,* **Daniel P. Scharf, Carl R. Seubert**,
and P. Doug Lisman
Jet Propulsion Laboratory, California Institute of Technology, Pasadena, California, United States

Abstract. NASA is studying a possible starshade flying in formation with the Nancy Grace Roman Space Telescope (Roman). The starshade would perform weeks-long translational retargeting maneuvers between target stars. A retargeting architecture that is based on chemical propulsion and does not require ground tracking or interactions with the telescope during the retargeting cruise is introduced. Feasibility is demonstrated through a covariance analysis of the starshade-telescope relative position over several weeks using realistic sensor and actuator assumptions. Performance is sufficient for Roman to reacquire the starshade after retargeting, and the architecture is shown to be applicable to other mission concepts such as the Habitable Exoplanet Observatory (HabEx). Results are verified through high-fidelity simulations, and driving sources of uncertainty are identified to confirm the robustness of the approach. © *2021 Society of Photo-Optical Instrumentation Engineers (SPIE)* [DOI: 10.1117/1.JATIS.7.2.021206]

Keywords: starshades; covariance analysis; uncertainty propagation.

Paper 20108SS received Jul. 31, 2020; accepted for publication Dec. 1, 2020; published online Jan. 6, 2021.

1 Introduction

1.1 *Starshades*

Starshades – large, precisely shaped, external occulters flying in formation with a telescope – offer a path to direct observation and spectroscopic characterization of Earth-like exoplanets (e.g. Refs. 1–4). Historical perspectives on starshades are included in Refs. 3 and 5. In the 2000s, flagship-class starshade missions were proposed (e.g., Refs. 6 and 7). In this decade, NASA starshade studies included both a Probe-class mission with a 20- to 30-m-diameter starshade that could rendezvous and operate with the Nancy Grace Roman Space Telescope ("Roman," see Refs. 1, 8, and 9) and a flagship-class mission, the Habitable Exoplanet Observatory ("HabEx," see Refs. 10 and 11) with a 52-m-diameter starshade.

A proposed operational concept for these missions, similar to Refs. 9 and 12–15 and shown in Fig. 1, would proceed as follows. First, the space telescope and the starshade spacecraft are inserted in similar quasi-halo orbits around the Second Sun-Earth Lagrange point (SEL2) using ground-based orbit determination (OD). After this initialization phase, a series of observations is performed by cycling through acquisition, science, and retargeting phases. The purpose of the acquisition phase is to align the starshade with respect to the telescope-star axis with sufficient precision to begin science observations. It includes handovers between three coboresighted telescope sensors with an increasingly fine resolution and narrow field of view (FOV): a coarse sensor (CS), an intermediate sensor (IS), and a fine sensor (FS). During the science phase, the two spacecraft are separated by tens of thousands of kilometers. Using FS measurements, the starshade uses its thrusters to maintain its meter-level alignment between the telescope and the star, for instance, as demonstrated in Refs. 12 and 15. At the end of the science phase, the starshade performs a retargeting maneuver to roughly position itself at the desired starshade-telescope distance in line with the next target star, as shown in Fig. 2. A new acquisition phase begins once the telescope reacquires the starshade with the CS at the end of of the retargeting cruise.

---

*Address all correspondence to Thibault L. B. Flinois, thibault.l.flinois@jpl.nasa.gov

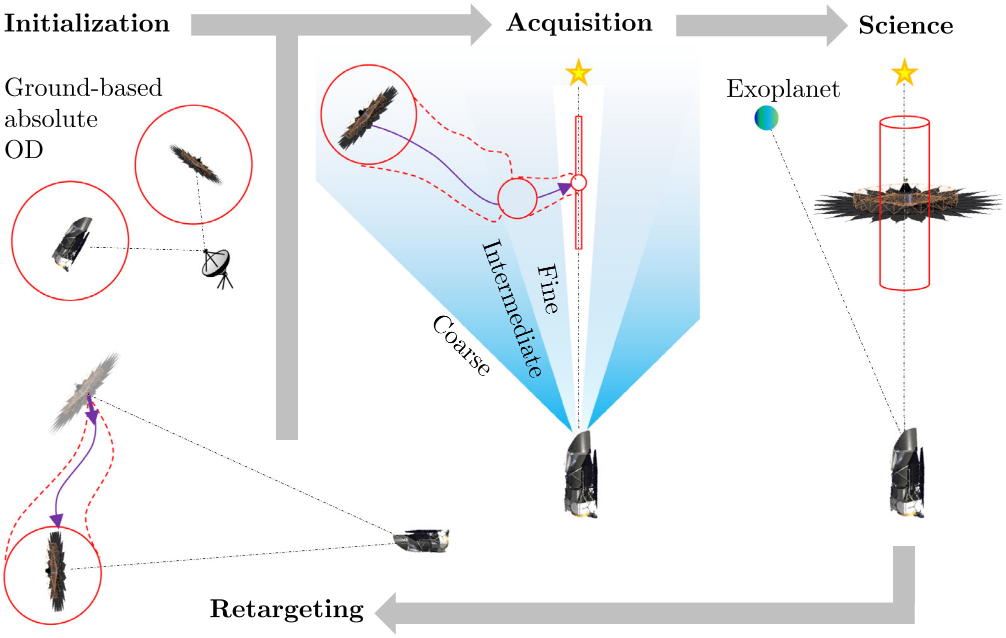

Fig. 1 Overview of a proposed concept of operations (not to scale). Figure adapted from Ref. 12.

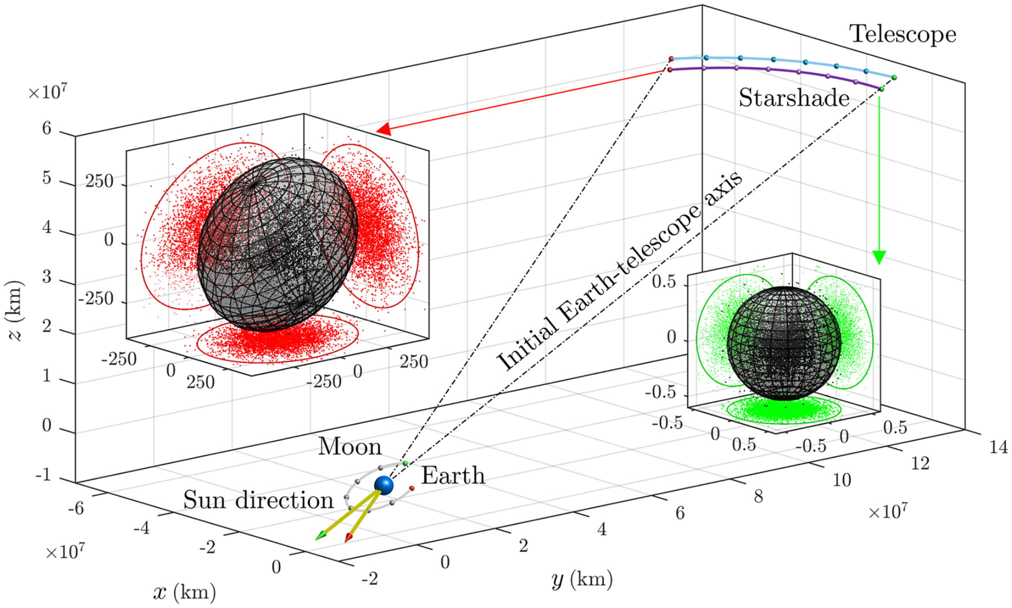

Fig. 2 Earth-relative visualization of the nominal scenario for lateral retargeting (defined in Sec. 4.3). Locations shown at 3-day intervals with initial locations in green and final in red. Right inset: visualization of initial relative position error $\delta\boldsymbol{\rho}_0$. Left inset: visualization of final retargeting error $\delta\boldsymbol{\rho}_f$ (see Sec 4.4). Point clouds show Monte Carlo results; ellipsoids and projections onto coordinate planes show 3σ covariance analysis predictions. The following scalings were applied to aid visualization: Earth-Moon distance increased 20×; Earth and Moon diameters increased 300×; and telescope-starshade distance increased 100×.

1.2 *Starshade Retargeting*

In this article, a guidance, navigation, and control achitecture is proposed for the retargeting phase, and its feasibility is demonstrated. For current starshade concepts (e.g., Refs. 9 and 11), the retargeting cruise can last several weeks, with initial Δvs as large as tens of meters-per-second. At the end of the cruise, position control of the starshade relative to the telescope must be sufficiently precise to ensure the starshade can be reacquired by the telescope's CS. The CS must also have sufficient resolution to hand over to the IS with its arcsecond-level FOV. As a result, a key constraint is that retargeting must be consistent with a degree-level CS FOV.

Apart from preliminary analyses such as Refs. 16 and 17, most previous approaches for retargeting are based on starshades with solar-electric propulsion (SEP) in an effort to reduce propellant mass and increase mission duration (e.g., Refs. 7, 8, 18 to 22). However, chemical propulsion (CP) is still likely required for starshade science as light emitted by continuously firing electric thrusters or sunlight reflected off their plumes could degrade observations. Relying on SEP for retargeting is therefore likely to lead to spacecraft designs with dual propulsion systems. In addition, high-power SEP systems require the starshade spacecraft to be fitted with significantly larger solar panels than for a CP-only design. Finally, measuring and correcting the low thrust of SEP with commercial off-the-shelf (COTS) on-board accelerometers with sufficient precision for reacquisition could be challenging. It might instead require comparatively expensive science-grade accelerometers or intermittent measurements of the starshade position from the ground, as in the Telescope for Habitable Exoplanets and Interstellar/Intergalactic Astronomy flagship study (THEIA, e.g., see Ref. 7). Alternatively, telescope operations could be interrupted at regular intervals during the cruise to acquire the starshade and measure its relative position, for instance, as in the Exo-S study (Ref. 8) or the New Worlds Observer concept (NWO, e.g., see Ref. 23).

1.3 *Proposed Retargeting Architecture*

In this article, a relatively less complex and inexpensive retargeting architecture is proposed, analyzed, and shown to be feasible. It consists of using only CP and a set of COTS accelerometers to perform an actively controlled retargeting Δv maneuver, followed by a passive cruise until reacquisition with the CS. Using an array of COTS accelerometers enables precise knowledge and therefore execution of the initial retargeting Δv. No additional SEP system is needed. Although a CP-only design is expected to have a higher propellant mass, this increase is partially offset by avoiding the need to carry an SEP system and the solar arrays to provide power for it (e.g., see Ref. 11). In addition, no science-grade accelerometers or intermittent sensor contacts from either the ground or the telescope are needed. Finally, the telescope does not need to perform a search with the CS at the end of the cruise: it is able to remain pointed at the star while its CS reacquires a starshade laser beacon (see Sec. 2 and, e.g., Ref. 14 for further details regarding relative bearing sensor concepts). These operational features could significantly reduce mission cost and complexity.

The feasibility of the proposed concept is demonstrated with a computationally efficient covariance propagation framework. This analytical approach evaluates the statistics of the retargeting error as well as its sensitivity to both nominal model parameters and uncertainty assumptions. Further insights into the error growth mechanisms are also provided, confirming the robustness of the retargeting architecture. Similar covariance analyses have been used in many prior studies for applications such as mission planning (Ref. 24), navigation (Refs. 25 and 26), descent and landing (Refs. 27 and 28), powered ascent (Ref. 29), and rendezvous and proximity operations (Refs. 30 and 31). In this article, the analysis is applied to both Roman-starshade and HabEx-starshade scenarios as representative examples. The results of these analyses show that in both cases a CS with a degree-level FOV is sufficient for reacquisition when using this CP-only retargeting architecture.

This article is structured as follows. In Sec. 2, based on the CP-only retargeting architecture and study of a possible starshade for Roman, a representative concept of operations (ConOps) for retargeting is described in detail. In Sec. 3, the covariance propagation framework is introduced. In Sec. 4, the framework is applied to the proposed retargeting concept for a Roman-starshade scenario, and the predictions are verified with Monte Carlo simulations for two stressing reference trajectories. A preliminary assessment is also conducted for a HabEx-starshade scenario. In Sec. 5, the error growth mechanisms are analyzed, and sensitivities to both nominal model parameters and uncertainty assumptions are computed. Finally, the conclusions of the work are given in Sec. 6. Some of the results presented in this article were also published in conference proceedings (Ref. 32).

2 Representative ConOps for CP-Only Architecture

In this section, a representative ConOps for CP-only retargeting, believed to be viable for starshades operating with Roman and HabEx, is described in detail. The main steps are summarized in Fig. 3, and key actuators and sensors are listed in Tables 1 and 2.

2.1 *Retargeting Initiation ($t_{\mathrm{sci}} \leqslant t \leqslant t_0$)*

At the end of the science phase ($t = t_{\mathrm{sci}}$), the two spacecraft are separated by tens of thousands of kilometers. The telescope has ended its starshade science observations and is pointing to the target star. Its absolute position is tracked at regular time intervals from the ground, and it performs monthly trajectory correction maneuvers (TCMs) to maintain its trajectory along its quasi-halo orbit. Starshade TCMs, performed with the starshade reaction control system (RCS) thrusters, are nominally identical to and synchronized with the telescope TCMs.

The starshade is spin-stabilized during the science phase and remains spin-stabilized throughout the retargeting phase (although the approach described here is expected to also apply to a three-axis stabilized starshade). Internal disturbances, solar radiation pressure (SRP) torque, and gravity gradient torques are sufficiently small not to require pointing maintenance

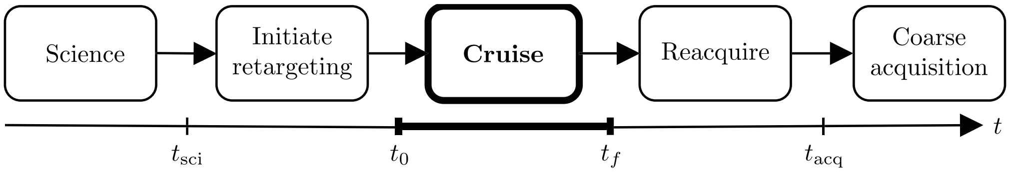

Fig. 3 Retargeting timeline. The covariance analysis focuses on the retargeting cruise, shown in bold.

Table 1 Representative starshade actuators and sensors used during retargeting.

Hardware	Function	Key characteristics
Main thrusters	Main retargeting burns	Aligned with axis of symmetry. Performance similar to Aerojet Rocketdyne R-6D.[33]
RCS thrusters	Other translational burns and slews	6 degree-of-freedom (DOF) control. Similar performance to main thrusters.
Array of COTS accelerometers	3-DOF acceleration sensing	Used while main or RCS thrusters are firing. Performance similar to Honeywell QA3000.[34]
Stellar reference units	Attitude sensing	Performance similar to Leonardo A-STR.[35]
S-band system	Longitudinal position sensing	500-m 3σ measurement accuracy. Also used for interspacecraft communications.
Laser beacon	Guiding signal for telescope sensors	Aligned with axis of symmetry. Degree-level beam width, sufficient power for reacquisition.

Table 2 Representative telescope actuators and sensors used during retargeting.

Hardware	Function	Key characteristics
CS	Starshade reacquisition	Custom, degree-level FOV camera. Aligned with telescope boresight. Also lateral position sensor for coarse acquisition phase.
S-band system	Longitudinal position sensing	500-m 3σ measurement accuracy. Also used for interspacecraft communications.

maneuvers during the retargeting cruise. The position of the starshade along the telescope-star axis, referred to as the relative longitudinal position, is measured by radio frequency ranging, using S-band systems installed on the two spacecraft. The FS is used to measure the relative lateral position (i.e., across the telescope-star axis) during the science phase and is still active at $t = t_{\mathrm{sci}}$ (e.g., see Refs. 12 and 15).

In this article, slews refer to pure spacecraft rotations. Between $t = t_{\mathrm{sci}}$ and $t = t_0$, the telescope slews with its reaction wheels and begins performing nonstarshade science. The starshade slews using its RCS thrusters to point its main thrusters in the retargeting burn direction, while remaining spin-stabilized and interrupting S-band and FS measurements. The main retargeting burn is performed with the starshade main thrusters to improve fuel efficiency by avoiding cosine losses. RCS thrusters and accelerometers are used in a closed loop during the main burn to reduce the execution error. A second slew is then performed to orient the starshade in the desired direction for the cruise. Finally, an open-loop burn is performed with RCS thrusters to correct remaining residuals measured with the accelerometers during the two slews and the main retargeting burn. Detailed modeling of these retargeting initiation maneuvers is included in Appendix A.

2.2 *Cruise ($t_0 \leqslant t \leqslant t_f$)*

At $t = t_0$, the telescope is performing nonstarshade science and the starshade is spin-stabilized and pointing in the chosen cruise direction. A maximum cruise duration of 3 weeks is considered representative, and some results are given for a cruise of up to 4 weeks. Nominally, no starshade thruster firings occur during the cruise except to potentially match a telescope TCM. For Roman, telescope reaction wheel desaturation maneuvers (desats) occur every 4 days (subject to change).

To prepare for reacquisition, the telescope ends nonstarshade science and slews with reaction wheels to point to the new starshade science target star. It then sets up its optical configuration for starshade acquisition and science. This procedure is done sufficiently early in the cruise to allow for thermal settling before reacquisition.

2.3 *Reacquisition ($t_f \leqslant t \leqslant t_{\mathrm{acq}}$)*

At $t = t_f$, the telescope is pointing to the new target star. When the starshade reaches the desired position relative to the telescope to initiate reacquisition, it slews using RCS thrusters toward the deceleration burn direction and uses its main thrusters to perform its main deceleration burn. It then slews with RCS thrusters to point to the target star, thus reestablishing S-band communications and relative longitudinal position sensing. It also turns on its laser beacon to enable reacquisition.

The telescope turns on the CS, which finds both the target star and the starshade laser beacon. At $t = t_{\mathrm{acq}}$, the starshade starts receiving relative bearing measurements from the CS, and the coarse acquisition phase begins.

3 Covariance Analysis Framework

In this section, the covariance propagation framework used to evaluate the feasibility of the proposed CP-only retargeting architecture is described.

3.1 *Notation and Problem Definition*

In the following paragraphs, the problem definition is stated and key notation, shown in Figure 4, is introduced. Initial time $t = t_0$ corresponds to the start of the cruise and is indicated with a “0” subscript. During reacquisition ($t_f \leqslant t \leqslant t_{\mathrm{acq}}$), the maneuvers that the starshade performs take place shortly before the CS finds the starshade beacon. Their influence on the relative position dispersion is therefore small. As a result, the final time $t = t_f$ corresponds to the end of the cruise phase ($t = t_f$) and is indicated with an “f” subscript.

The telescope and starshade absolute positions, expressed in an inertial reference frame, are $\boldsymbol{r}(t)$ and $\boldsymbol{s}(t)$, respectively, where t represents time. The relative position of the starshade with respect to the telescope is $\boldsymbol{\rho}(t) = \boldsymbol{s}(t) - \boldsymbol{r}(t)$.

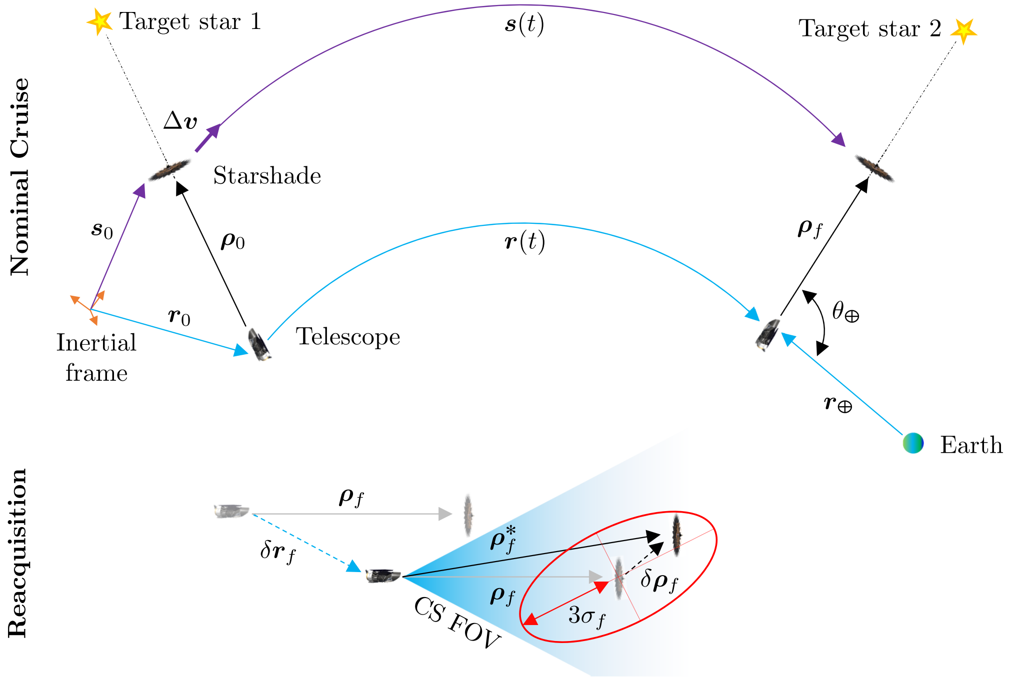

Fig. 4 Illustration of the retargeting phase. Top: nominal cruise; bottom: reacquisition (not to scale).

Scalars such as vector norms are denoted in roman italic font; for instance, $\rho = \|\boldsymbol{\rho}\|$. Unit vectors are denoted with a "hat"; for instance, $\hat{\boldsymbol{\rho}} = \boldsymbol{\rho}/\rho$. Time derivatives are indicated with a "dot"; for instance, $\dot{\boldsymbol{\rho}} = d\boldsymbol{\rho}/dt$. The matrix I is an identity matrix, and the matrix $0_{n\times m}$ is an $(n \times m)$ zero matrix. The subscript is omitted for square matrices $(n = m)$.

The nominal value of a variable corresponds to its current best estimate (CBE). In some cases, the nominal values are obtained from a combination of measurements, estimation, and propagation; in others, they are known by design (e.g., commanded values of Δvs). The error in a variable's value, denoted with a "δ," is the difference between the true value, denoted with an asterisk, and the nominal value of the variable. For instance, the relative position error is $\delta\boldsymbol{\rho} = \boldsymbol{\rho}^* - \boldsymbol{\rho}$. As such, the true values are random variables, and unless specified otherwise, their expected value is equal to their nominal value; for instance, $E(\boldsymbol{\rho}^*) = \boldsymbol{\rho}$. Covariance matrices thus represent the spread of possible true values about the nominal value. For example, the covariance matrix of the relative position error is $\mathrm{Cov}(\delta\boldsymbol{\rho}, \delta\boldsymbol{\rho}) = \mathrm{Cov}(\delta\boldsymbol{\rho}) = E(\delta\boldsymbol{\rho}\delta\boldsymbol{\rho}^\dagger)$, where † is the Hermitian transpose operation.

For the proposed architecture to be feasible, it is not sufficient to bound the final relative position knowledge error: the final retargeting error itself must be sufficiently small. In addition, for infinitely far target stars, the ability to successfully reacquire only depends on the relative position error at the end of the cruise $\delta\boldsymbol{\rho}_f$. It does not depend on the final absolute position of the telescope $\delta\boldsymbol{r}_f$ and starshade $\delta\boldsymbol{s}_f$ explicitly. However, they must be considered in the analysis because the growth of $\delta\boldsymbol{\rho}$ during the cruise does depend on the absolute position errors, as discussed below.

3.2 *Sources of Uncertainty*

In this section, the sources of uncertainty included in the analysis are described. At the start of the cruise, when $t = t_0$, the errors in the initial telescope, starshade, and relative states are $[\delta\boldsymbol{r}_0^\dagger, \delta\dot{\boldsymbol{r}}_0^\dagger]^\dagger$, $[\delta\boldsymbol{s}_0^\dagger, \delta\dot{\boldsymbol{s}}_0^\dagger]^\dagger$, and $[\delta\boldsymbol{\rho}_0^\dagger, \delta\dot{\boldsymbol{\rho}}_0^\dagger]^\dagger$. respectively. First, the initial state errors are subject to the guidance error. This error source appears because the commanded retargeting burn is designed based on the nominal system state at the end of the science phase (i.e., when $t = t_{\mathrm{sci}}$). However, because of the knowledge error in the true absolute and relative states at $t = t_{\mathrm{sci}}$, the designed burn is not perfect in general. Even in the absence of all other sources of uncertainty described in this section, there would still be a nonzero guidance error. Second, the initial state errors are affected by residuals from the main starshade retargeting burn. Third, a TCM is conservatively assumed to occur at $t = t_0$ to maximize the propagation time of associated burn residuals. Additional TCMs could also be addressed, but they are only expected at a monthly cadence.

During the cruise, when $t_0 \leqslant t \leqslant t_f$, these initial state errors propagate through SEL2 gravity gradients. In addition, the growth of telescope, starshade, and relative state errors, given by $[\delta\boldsymbol{r}^\dagger(t), \delta\dot{\boldsymbol{r}}^\dagger(t)]^\dagger$, $[\delta\boldsymbol{s}^\dagger(t), \delta\dot{\boldsymbol{s}}^\dagger(t)]^\dagger$, and $[\delta\boldsymbol{\rho}^\dagger(t), \delta\dot{\boldsymbol{\rho}}^\dagger(t)]^\dagger$, respectively, is further exacerbated by residuals from telescope desats and uncertainty in SRP acceleration. The relative SRP acceleration uncertainty is $\delta\ddot{\boldsymbol{\rho}}_{\text{SRP}} = \delta\ddot{\boldsymbol{s}}_{\text{SRP}} - \delta\ddot{\boldsymbol{r}}_{\text{SRP}}$.

All sources of uncertainty that contribute to the final relative position dispersion are listed in Table 3 and shown in Fig. 5. The numerical values in the table are representative of a Roman-starshade scenario and are discussed in Sec. 4.

Table 3 Retargeting sources of uncertainty.

Source of uncertainty	Error symbol	Standard deviation symbol	Standard deviation value
Relative position error at $t = t_{\text{sci}}$	$\delta\boldsymbol{\rho}_{\text{sci}}$	$\sigma_{\delta\rho,\text{sci}}$	167 m
Telescope absolute position error at $t = t_{\text{sci}}$	$\delta\boldsymbol{r}_{\text{sci}}$	$\sigma_{\delta r,\text{sci}}$	33.3 km
Relative velocity error at $t = t_{\text{sci}}$	$\delta\dot{\boldsymbol{\rho}}_{\text{sci}}$	$\sigma_{\delta\dot{\rho},\text{sci}}$	33.3 mm/s
Telescope absolute velocity error at $t = t_{\text{sci}}$	$\delta\dot{\boldsymbol{r}}_{\text{sci}}$	$\sigma_{\delta\dot{r},\text{sci}}$	33.3 mm/s
Residuals from starshade TCM	$\delta\dot{\boldsymbol{s}}_{\text{TCM}}$	$\sigma_{\delta\dot{s},\text{TCM}}$	6.0 mm/s
Residuals from telescope TCM	$\delta\dot{\boldsymbol{r}}_{\text{TCM}}$	$\sigma_{\delta\dot{r},\text{TCM}}$	2.33 mm/s
Residuals from main starshade retargeting burns/slews	$\delta\dot{\boldsymbol{s}}_{\text{ret}}$	$\sigma_{\delta\dot{s},\text{ret}}$	40 mm/s
Residuals from each telescope desat	$\delta\dot{\boldsymbol{r}}_{\text{desat}}$	$\sigma_{\delta\dot{r},\text{desat}}$	1.33 mm/s
Uncertainty in starshade SRP acceleration	$\delta\ddot{\boldsymbol{s}}_{\text{SRP}}$	$\sigma_{\delta\ddot{s},\text{SRP}}$	40 nm/s^2
Uncertainty in telescope SRP acceleration	$\delta\ddot{\boldsymbol{r}}_{\text{SRP}}$	$\sigma_{\delta\ddot{r},\text{SRP}}$	5 nm/s^2

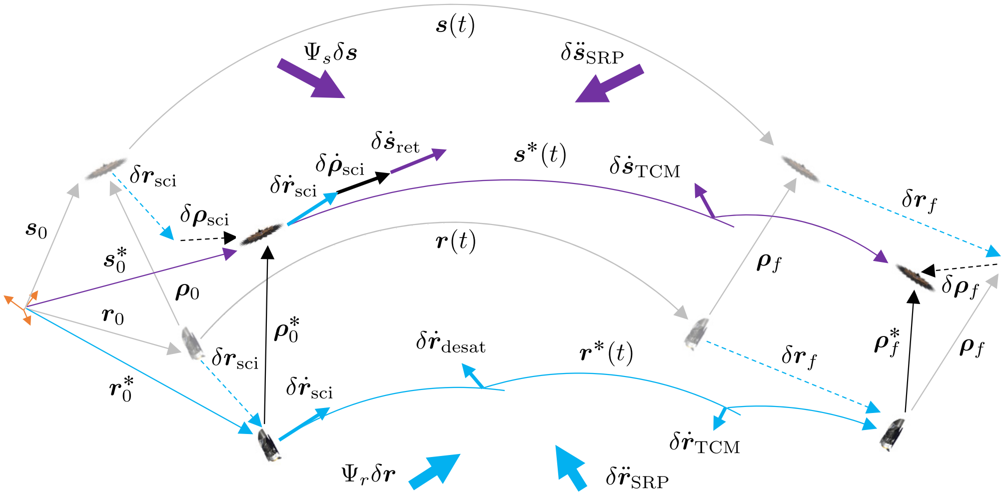

Fig. 5 Illustration of retargeting sources of uncertainty. Thin lines: position vectors; thick lines: velocity vectors; very thick lines: acceleration vectors; dashed lines: error position vectors; blue: telescope quantities; purple: starshade quantities; black: relative quantities; gray: nominal quantities (not to scale).

3.3 *Error Dynamics Formulation*

Having listed the relevant sources of uncertainty, the linearized error dynamics are derived in Sec. 3.4 using the approach described in this section. In particular, three distinct features of the error dynamics formulation are highlighted.

The first feature is that error dynamics are linearized about given absolute trajectories for both the telescope and the starshade, $\boldsymbol{r}(t)$ and $\boldsymbol{s}(t)$, respectively. Note that a given relative trajectory for the starshade, $\boldsymbol{\rho}(t)$, such that $\boldsymbol{s}(t) = \boldsymbol{r}(t) + \boldsymbol{\rho}(t)$ could also be used. An absolute trajectory is chosen here for clarity and convenience. Whereas absolute position errors of 100s of kilometers are expected, SEL2 is more than 1,000,000 km from the Earth and Moon. For both spacecraft, the choice to linearize about $\boldsymbol{r}(t)$ and $\boldsymbol{s}(t)$ is therefore justified, and the validity of the approach is further confirmed via Monte Carlo simulations in Sec. 4. The major advantage of this approach is that the accuracy is effectively independent of the telescope–starshade distance. As a result, this covariance propagation framework is broadly applicable for retargeting analyses. An alternative would be to linearize both the telescope true position and starshade true position about the telescope reference trajectory as in Ref. 36. However, the telescope–starshade distance can be close to a 100,000 km, so the linearization errors may not be negligible in this case.

Thus, starting from the nominal initial state vectors (at $t = t_0$), telescope and starshade absolute positions $\boldsymbol{r}(t)$ and $\boldsymbol{s}(t)$ are propagated and stored for $t_0 \leqslant t \leqslant t_f$ using a fixed time-step fifth-order Runge–Kutta ordinary differential equation solver. This solver was validated against MONTE simulations[37] (MONTE is the JPL's high-fidelity mission design tool, validated operationally on several NASA deep space missions, including Cassini, Mars Science Laboratory, and Juno) and used in Ref. 12. This MATLAB®-based environment propagates the position of a telescope and a starshade spacecraft in three-dimensional space, under the influence of the gravity from the Earth, Sun, Moon, and SRP. Rather than exactly matching a particular Design Reference Mission (DRM), trajectories representative of a Roman-starshade scenario (Ref. 9) that stress the feasibility of reacquisition are sought. The chosen reference trajectories are described and discussed in Sec. 4.3.

The second feature is that after linearization about $\boldsymbol{r}(t)$ and $\boldsymbol{s}(t)$, the equations are reformulated to be explicit in the dynamics of the relative state error, $\delta\boldsymbol{\rho}$. This reformulation has two objectives. First, the final relative retargeting error $\delta\boldsymbol{\rho}_f$ is what determines the feasibility of the retargeting architecture. Therefore, it is sensible to propagate its covariance directly rather than that of $\delta\boldsymbol{s}$. Second, integrating $\delta\boldsymbol{\rho}$ directly instead of $\delta\boldsymbol{s}$ takes advantage of the fact that at $t = t_{\mathrm{sci}}$, the relative position errors (~0.1 km) are orders of magnitude smaller than the absolute position errors (~100 km).

The final feature is that the chosen formulation shows that the growth in $\delta\boldsymbol{\rho}$ is relatively insensitive to the absolute telescope position errors. Specifically, $\delta\boldsymbol{r}$ only appears as a second-order error in the gravity-gradient: compare the absolute position errors of 100s of kilometers with a distance of more than 1,000,000 km from SEL2 to the Earth and Moon.

3.4 *Error Dynamics Derivation*

The dynamics of the telescope position error $\delta\boldsymbol{r}(t)$, once linearized about its reference trajectory $\boldsymbol{r}(t)$, can be shown to be (e.g., Ref. 38):

$$\delta\ddot{\boldsymbol{r}} = \sum_{\text{bodies } i} \frac{-\mu_i}{r_i^3}(I - 3\hat{\boldsymbol{r}}_i\hat{\boldsymbol{r}}_i\ )\delta\boldsymbol{r} + \delta\ddot{\boldsymbol{r}}_{\mathrm{SRP}} = \Psi_r\delta\boldsymbol{r} + \delta\ddot{\boldsymbol{r}}_{\mathrm{SRP}}, \tag{1}$$

where $\delta\ddot{\boldsymbol{r}}_{\mathrm{SRP}}$ is the telescope SRP acceleration error and $\boldsymbol{r}_i(t)$ is the vector from the i'th gravitational body with gravitational constant μ_i to the telescope, computed from the stored reference absolute trajectory $\boldsymbol{r}(t)$. An analogous equation is written for the starshade, leading to $\delta\ddot{\boldsymbol{s}} = \Psi_s\delta\boldsymbol{s} + \delta\ddot{\boldsymbol{s}}_{\mathrm{SRP}}$. The linearized relative error dynamics are thus

$$\delta\ddot{\boldsymbol{\rho}} = \delta\ddot{\boldsymbol{s}} - \delta\ddot{\boldsymbol{r}} = (\Psi_s - \Psi_r)\delta\boldsymbol{r} + \Psi_s\delta\boldsymbol{\rho} + \delta\ddot{\boldsymbol{\rho}}_{\mathrm{SRP}}. \tag{2}$$

Although the dependence on t is not shown explicitly in the equations above for readability, $\Psi_r(t)$ and $\Psi_s(t)$ are time-varying matrices. They are functions of the absolute nominal positions at time t of the two spacecraft as they travel along their reference trajectories.

In addition, the telescope performs desats at fixed time intervals Δt_{desat}. The residuals from these maneuvers are modeled as acceleration error impulses, leading to the following state-space system:

$$\begin{bmatrix} \delta\dot{\boldsymbol{\rho}} \\ \delta\dot{\boldsymbol{r}} \\ \delta\ddot{\boldsymbol{\rho}} \\ \delta\ddot{\boldsymbol{r}} \\ \delta\boldsymbol{\rho}_{\text{SRP}} \\ \delta\boldsymbol{r}_{\text{SRP}} \end{bmatrix} = \begin{bmatrix} 0 & I & 0 \\ A_{\Psi} & 0 & I \\ 0 & 0 & 0 \end{bmatrix} \begin{bmatrix} \delta\boldsymbol{\rho} \\ \delta\boldsymbol{r} \\ \delta\dot{\boldsymbol{\rho}} \\ \delta\dot{\boldsymbol{r}} \\ \delta\ddot{\boldsymbol{\rho}}_{\text{SRP}} \\ \delta\ddot{\boldsymbol{r}}_{\text{SRP}} \end{bmatrix} + \begin{bmatrix} 0_{6\times3} \\ G_{\text{desat}} \\ 0_{6\times3} \end{bmatrix} \delta\dot{\boldsymbol{r}}_{\text{desat}}, \tag{3}$$

where

$$A_{\Psi} = \begin{bmatrix} \Psi_s & (\Psi_s - \Psi_r) \\ 0 & \Psi_r \end{bmatrix}, \quad G_{\text{desat}} = \begin{bmatrix} I \\ I \end{bmatrix}. \tag{4}$$

In Eq. (3), $\delta\ddot{\boldsymbol{\rho}}_{\text{SRP}}$ and $\delta\ddot{\boldsymbol{r}}_{\text{SRP}}$ remain constant. These SRP uncertainty terms are included in the state rather than added as an external input for mathematical convenience. Equation (3) is in the standard continuous linear time varying state-space form:

$$\dot{\boldsymbol{x}}(t) = A(t)\boldsymbol{x}(t) + G\boldsymbol{w}(t), \tag{5}$$

where $\boldsymbol{x}(t)$ is the state vector, $\boldsymbol{w}(t) = \delta\dot{\boldsymbol{r}}_{\text{desat}}(t)$ is the state disturbance vector, $A(t)$ is the state matrix, and G is the state disturbance matrix. The disturbances $\delta\dot{\boldsymbol{r}}_{\text{desat}}(t)$ are trains of vector impulses taking place at constant time intervals Δt_{desat}, conservatively starting at $t = t_0$. The components of each impulse vector in the train are zero-mean normally distributed uncorrelated random variables, such that the vector covariance matrix is $\sigma^2_{\delta\dot{r},\text{desat}} I$.

Once discretized, the dynamics become

$$\boldsymbol{x}_{k+1} = \Phi_k \boldsymbol{x}_k + \Gamma \boldsymbol{w}_k. \tag{6}$$

Here, $\boldsymbol{x}_k$ is the discretized state vector and $\Phi_k = \exp[A(t_k)\Delta t]$ is the discretized state transition matrix, where Δt is the time step and $t_k = k\Delta t$. The discretized state disturbance vector $\boldsymbol{w}_k$ is a train of regularly spaced pulses. The components of each pulse vector in the train are zero-mean normally distributed uncorrelated random variables, such that the vector covariance matrix is again $\sigma^2_{\delta\dot{r},\text{desat}} I$. Because of the impulsive nature of the inputs, the discretized state disturbance matrix can be shown to be $\Gamma = G$.

3.5 *Covariance Propagation*

The system output is chosen to be $\boldsymbol{y}(t) = C\boldsymbol{x}(t) = \delta\boldsymbol{\rho}(t)$, where $C = [I, 0_{3\times15}]$ is the output matrix. The statistics of the final relative position error are thus given by the final output covariance matrix:

$$P_{y,f} = \text{Cov}(\boldsymbol{y}_f) = CP_fC^{\dagger}, \tag{7}$$

where $P_f = \text{Cov}(\boldsymbol{x}_f)$ is the covariance matrix of the state at the end of the cruise.

In this study, the following quantity is used to evaluate retargeting performance:

$$\sigma_f = \sqrt{\mathfrak{s}_{y1}}, \tag{8}$$

where $\mathfrak{s}_{y1}$ is the largest singular value of $P_{y,f}$. Physically, the scalar σ_f is the length of the largest semi-major axis of the ellipsoid defined by $P_{y,f}$ (see Fig. 4). Noting that the norm $\delta\rho_f$ follows a chi distribution rather than a normal distribution, σ_f is used to size the CS FOV. For instance, the analysis predicts that, at $t = t_f$, the starshade will be inside a CS FOV of radius $3\sigma_f$ with 97.1%

confidence. This confidence value corresponds to the worst-case direction, associated with σ_f, and is therefore a lower bound.

Starting from the initial state covariance matrix P_0, the final state covariance matrix P_f is evaluated by propagating the state covariance matrix $P_k = \mathrm{Cov}(\boldsymbol{x}_k)$ using

$$P_{k+1} = \Phi_k P_k \Phi_k^\dagger + \Gamma Q_k \Gamma^\dagger, \tag{9}$$

where Q_k is the covariance matrix of $\boldsymbol{w}_k$:

$$Q_k = \mathrm{Cov}(\boldsymbol{w}_k) = \sigma^2_{\mathrm{desat},k} I. \tag{10}$$

Here, $\sigma_{\mathrm{desat},k} = \sigma_{\delta\dot{r},\mathrm{desat}}$ if t_k is a multiple of $\Delta t_{\mathrm{desat}}$, and $\sigma_{\mathrm{desat},k} = 0$ otherwise.

The matrix P_0 provides the statistics of the initial state $\boldsymbol{x}_0$, which has the following components. Initial absolute state errors are

$$\delta\boldsymbol{r}_0 = \delta\boldsymbol{r}_{\mathrm{sci}}, \quad \delta\dot{\boldsymbol{r}}_0 = \delta\dot{\boldsymbol{r}}_{\mathrm{sci}} + \delta\dot{\boldsymbol{r}}_{\mathrm{TCM}}, \tag{11}$$

and initial relative state errors are

$$\delta\boldsymbol{\rho}_0 = \delta\boldsymbol{\rho}_{\mathrm{sci}}, \quad \delta\dot{\boldsymbol{\rho}}_0 = \delta\dot{\boldsymbol{\rho}}_{\mathrm{sci}} + \delta\dot{\boldsymbol{s}}_{\mathrm{ret}} + \delta\dot{\boldsymbol{s}}_{\mathrm{TCM}} - \delta\dot{\boldsymbol{r}}_{\mathrm{TCM}}. \tag{12}$$

The associated covariance matrices are

$$\mathrm{Cov}(\delta\boldsymbol{r}_0) = \sigma^2_{\delta\boldsymbol{r},\mathrm{sci}} I, \quad \mathrm{Cov}(\delta\dot{\boldsymbol{r}}_0) = \sigma^2_{\delta\dot{\boldsymbol{r}},\mathrm{sci}} I + \sigma^2_{\delta\dot{\boldsymbol{r}},\mathrm{TCM}} I, \tag{13}$$

$$\mathrm{Cov}(\delta\boldsymbol{\rho}_0) = \sigma^2_{\delta\boldsymbol{\rho},\mathrm{sci}} I, \quad \mathrm{Cov}(\delta\dot{\boldsymbol{\rho}}_0) = \sigma^2_{\delta\dot{\boldsymbol{\rho}},\mathrm{sci}} I + \sigma^2_{\delta\dot{\boldsymbol{s}},\mathrm{ret}} I + \sigma^2_{\delta\dot{\boldsymbol{s}},\mathrm{TCM}} I + \sigma^2_{\delta\dot{\boldsymbol{r}},\mathrm{TCM}} I, \tag{14}$$

$$\mathrm{Cov}(\delta\boldsymbol{\rho}_0, \delta\boldsymbol{r}_0) = 0, \quad \mathrm{Cov}(\delta\dot{\boldsymbol{\rho}}_0, \delta\dot{\boldsymbol{r}}_0) = -\sigma^2_{\delta\dot{\boldsymbol{r}},\mathrm{TCM}} I. \tag{15}$$

The covariance matrices of SRP uncertainties are

$$\mathrm{Cov}(\delta\ddot{\boldsymbol{r}}_{\mathrm{SRP},0}) = -\mathrm{Cov}(\delta\ddot{\boldsymbol{\rho}}_{\mathrm{SRP},0}, \delta\ddot{\boldsymbol{r}}_{\mathrm{SRP},0}) = \sigma^2_{\delta\ddot{\boldsymbol{r}},\mathrm{SRP}} I, \quad \mathrm{Cov}(\delta\ddot{\boldsymbol{\rho}}_{\mathrm{SRP},0}) = \sigma^2_{\delta\ddot{\boldsymbol{s}},\mathrm{SRP}} I + \sigma^2_{\delta\ddot{\boldsymbol{r}},\mathrm{SRP}} I. \tag{16}$$

The resulting initial state covariance matrix P_0 is

$$P_0 = \begin{bmatrix} \sigma^2_{\delta\boldsymbol{\rho},\mathrm{sci}} I & 0 & 0 & 0 & 0 & 0 \\ 0 & \sigma^2_{\delta\boldsymbol{r},\mathrm{sci}} I & 0 & 0 & 0 & 0 \\ 0 & 0 & \mathrm{Cov}(\delta\dot{\boldsymbol{\rho}}_0) & -\sigma^2_{\delta\dot{\boldsymbol{r}},\mathrm{TCM}} I & 0 & 0 \\ 0 & 0 & -\sigma^2_{\delta\dot{\boldsymbol{r}},\mathrm{TCM}} I & \mathrm{Cov}(\delta\dot{\boldsymbol{r}}_0) & 0 & 0 \\ 0 & 0 & 0 & 0 & \sigma^2_{\delta\ddot{\boldsymbol{\rho}},\mathrm{SRP}} I & -\sigma^2_{\delta\ddot{\boldsymbol{r}},\mathrm{SRP}} I \\ 0 & 0 & 0 & 0 & -\sigma^2_{\delta\ddot{\boldsymbol{r}},\mathrm{SRP}} I & \sigma^2_{\delta\ddot{\boldsymbol{r}},\mathrm{SRP}} I \end{bmatrix}. \tag{17}$$

4 Covariance Analysis Results

In this section, the framework introduced above is applied to a Roman-starshade scenario. Assumptions leading to the uncertainty values in Table 3 and to the choice of reference trajectories are first described. Corresponding covariance analysis results, including the verification of the framework accuracy through Monte Carlo simulations, are then discussed. Finally, a preliminary assessment is conducted for a HabEx-starshade scenario.

4.1 *Conservatism in Assumptions*

This work focuses on introducing a covariance propagation framework for starshade retargeting that is capable of authoritatively evaluating retargeting error statistics. It also shows that, for stressing and representative parameters, including actuator and sensor performance, the proposed retargeting architecture is feasible.

One of the conservative assumptions made in this article is that, even though many sources of uncertainty are anisotropic (for instance, the retargeting burn execution error, discussed in Appendix A), the uncertainty associated with the worst-case direction is applied to every axis. Some of the nominal parameters chosen in the sections below are also more conservative than expected for either a Roman or a HabEx starshade scenario. Finally, σ_f is conservatively used as the main retargeting performance metric.

These simplifications reduce the number of parameters in the analysis, which allows for making bounding arguments about the retargeting error and generates valuable intuition about the system. For any specific DRM, however, the covariance propagation tool is able to incorporate the directionality associated with the initial conditions of each retargeting burn in the sequence and provide tailored retargeting performance estimates. This step will be addressed as part of future work.

4.2 *Selection of Uncertainty Parameters*

The standard deviations of the science-phase relative position $\sigma_{\delta\boldsymbol{\rho},\mathrm{sci}}$ and velocity $\sigma_{\delta\dot{\boldsymbol{\rho}},\mathrm{sci}}$ in Table 3 are based on the expected science sensing performance for a starshade operating with Roman (e.g., Refs. 9, 12, and 15). The science-phase relative lateral sensing performance is tens of centimeters in position and millimeters per second in velocity. By contrast, the relative longitudinal sensing performance is hundreds of meters in position and centimeters per second in velocity. As discussed in Sec. 4.1, the more conservative longitudinal values are used for all axes.

Based on communications with the Roman navigation team about the design of the telescope and its operations at the time of writing, the conservative estimates of $\sigma_{\delta\boldsymbol{r},\mathrm{sci}}$, $\sigma_{\delta\dot{\boldsymbol{r}},\mathrm{sci}}$, $\sigma_{\delta\dot{\boldsymbol{r}},\mathrm{TCM}}$, $\sigma_{\delta\dot{\boldsymbol{r}},\mathrm{desat}}$, and $\sigma_{\delta\ddot{\boldsymbol{r}},\mathrm{SRP}}$ were generated (see Table 3). These values do not explicitly reflect Roman telescope requirements and are subject to change.

In this analysis, the residuals from each desat are assumed to be uncorrelated. In practice, some correlation might exist if the telescope pointing direction remains fixed while performing nonstarshade-related science for a large portion of the cruise. The execution error corresponding to the starshade retargeting burns and slews $\delta\dot{\boldsymbol{s}}_{\mathrm{ret}}$ is discussed in detail and evaluated in Appendix A. The starshade TCM residual uncertainty is estimated using the open-loop performance of the RCS thrusters, also discussed in Appendix A.

To select $\sigma_{\delta\ddot{\boldsymbol{s}},\mathrm{SRP}}$, the following model for the SRP acceleration due to a Sun-facing specularly reflective plate of surface area error $\delta\mathcal{S}_{\mathrm{SRP}}$ is used (e.g., Refs. 39 and 40): $\delta\ddot{\boldsymbol{r}}_{\mathrm{SRP}} = [2\phi\delta\mathcal{S}_{\mathrm{SRP}}/(mc)]\hat{\boldsymbol{r}}_{\odot}$. Here, $\hat{\boldsymbol{r}}_{\odot}$ is the unit vector pointing from the Sun to the spacecraft, ϕ is the solar flux at a given distance between the spacecraft and the Sun, m is the spacecraft mass, and c is the speed of light in vacuum. As ϕ, m, and c are approximately constant during the cruise, $\delta\mathcal{S}_{\mathrm{SRP}}$ is the only independent variable. Its standard deviation, denoted $\sigma_{\mathcal{S}}$, thus provides an intuitive means of estimating representative SRP uncertainty magnitudes.

In this analysis, the cruise is performed with the starshade facing the Sun. In practice, the cruise attitude would be determined by a system trade including, e.g., power, thermal, SRP, micrometeorites, and communications considerations. For a Roman starshade (Ref. 9), the full starshade frontal area is 335 m^2. Despite its size, the starshade frontal area is precisely characterized for science purposes. Extensive in-orbit calibrations may also be performed on the deployed starshade during commissioning as it travels from Earth to SEL2. Based on these considerations, the chosen value of $\sigma_{\delta\ddot{\boldsymbol{s}},\mathrm{SRP}} = 40\ \mathrm{nm/s}^2$ corresponds to a nominal standard deviation of 0.5% of the total frontal area. This value of $\sigma_{\mathcal{S}}$ is conservative: for non-Sun-facing starshade cruise attitudes, it represents a larger percentage of the total Sun-facing area.

4.3 *Selection of Reference Trajectories*

The linear dynamics operators Ψ_s and Ψ_r in Eq. (4) are functions of the reference trajectories as they depend on the distances between the two spacecraft and each gravitational body at every point during the cruise. In this section, two full retargeting trajectories designed to be representative and stress the feasibility of the proposed retargeting architecture are presented. The sensitivity of the retargeting error to the nominal trajectory parameters is further discussed in

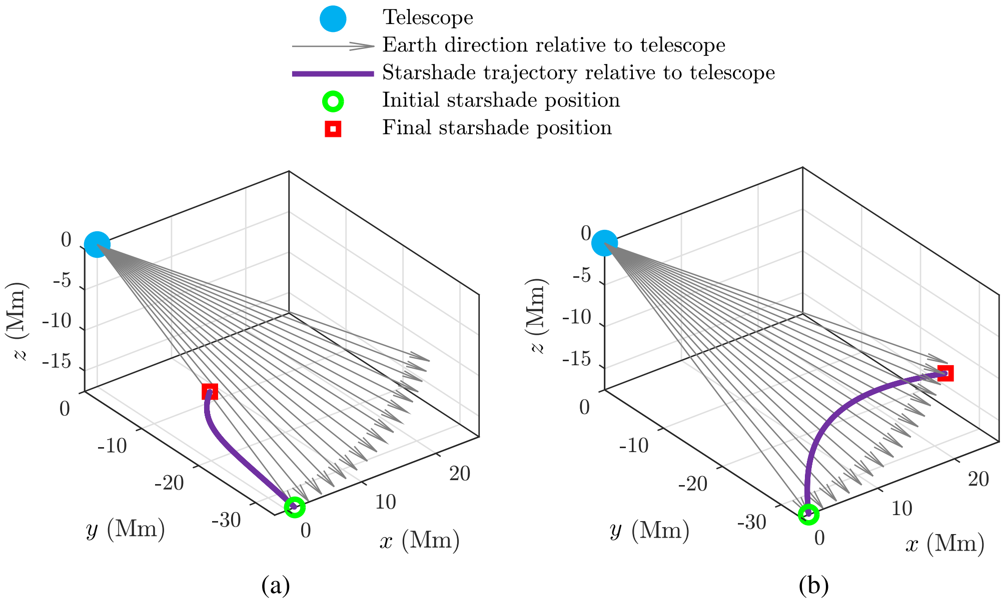

Fig. 6 Reference retargeting trajectories relative to telescope position. (a) Longitudinal retargeting maneuver. (b) Lateral retargeting maneuver.

Sec. 5. Several methods exist for optimizing DRMs and starshade trajectories with given initial and final conditions (e.g., Refs. 41 to 43). Because this work focuses on feasibility rather than on a specific DRM, stressing initial and desired final conditions are selected and a retargeting burn that approximately satisfies these boundary conditions is found by trial-and-error.

For both reference trajectories, starting from a representative Roman trajectory provided by the Roman navigation team, the initial telescope–Earth distance is minimized ($r_{\oplus,0}$ close to 1200 Mm), and the starshade is initially positioned along the telescope–Earth axis, as close to Earth as possible: $\rho_0 = 37.7$ Mm (maximum distance mentioned in Ref. 9) and $\theta_\oplus = 0^\circ$. The Earth formation angle $\theta_\oplus$ is defined as the angle between $-\boldsymbol{r}_\oplus$ and $\boldsymbol{\rho}$ (see Fig. 4). Although neither a Roman nor a HabEx scenario would allow for $\theta_\oplus = 0°$, the relative position vector has a secondary influence on the error dynamics, as discussed in Sec. 5.2.2. For this reason, $\theta_\oplus = 0°$ is chosen for conservatism and simplicity (see Sec. 4.1). Both retargeting cruises last 3 weeks (again, consistent with Ref. 9), and both trajectories remain approximately in the plane defined by the telescope position, the Earth position, and the telescope velocity vector relative to Earth over the entire cruise.

The first trajectory is a longitudinal retargeting maneuver. It is designed so that the inertial direction of the formation is approximately unchanged at the end of the cruise $\hat{\boldsymbol{\rho}}_f \approx \hat{\boldsymbol{\rho}}_0$ and the final telescope–starshade distance is $\rho_f \approx 21.3$ Mm. This trajectory is chosen because minimizing the final telescope–starshade distance leads to the most stringent retargeting error requirement (in kilometers) for a given CS angular FOV. The magnitude of this burn is 19.5 m/s. The starshade trajectory relative to the telescope is shown in Fig. 6(a).

The second trajectory is a lateral retargeting maneuver. It is designed to lead to an ~40° retargeting angle between $\hat{\boldsymbol{\rho}}_0$ and $\hat{\boldsymbol{\rho}}_f$, while keeping the initial and final longitudinal distance approximately constant: $\rho_f \approx \rho_0 = 37.7$ Mm. This trajectory is chosen because large values of ρ increase the retargeting error, as shown in Secs. 5.2.2 and 5.2.3. The magnitude of this burn is 20 m/s. The starshade trajectory relative to the telescope is shown in Fig. 6(b), and both the telescope and starshade trajectories relative to Earth are shown in Fig. 2.

4.4 *Results*

Figure 7(a) shows the evolution of σ_f as a function of the cruise duration for the two time-varying reference trajectories. It also compares them with the bounding time-invariant system defined in Sec. 5.2.4. As expected, both reference trajectories lead to slightly smaller final retargeting errors

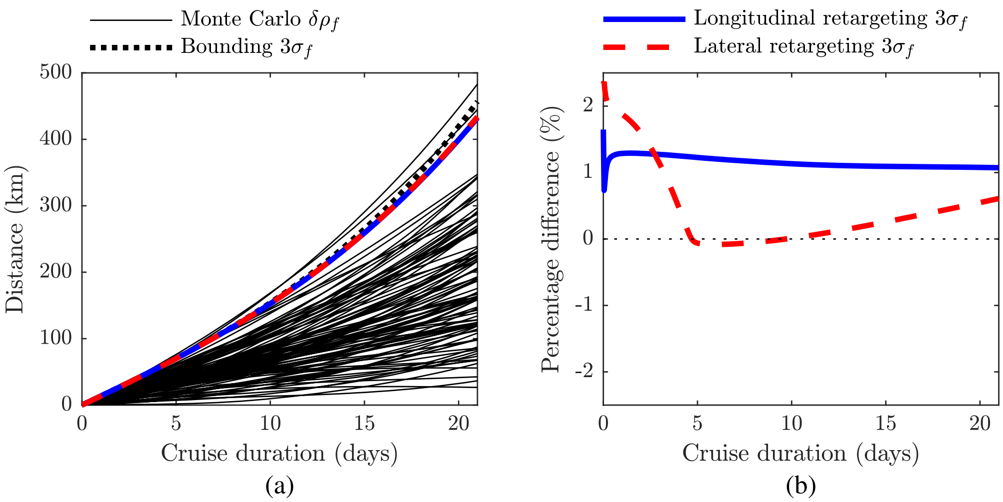

Fig. 7 (a) Retargeting $3\sigma_f$ error as a function of t_f for both the longitudinal and the lateral retargeting trajectories, as predicted by the covariance analysis. The evolution of $\delta\rho(t)$ for the longitudinal retargeting maneuver is also shown for 100 out of the 5000 Monte Carlo trajectories. The value of $3\sigma_f$ for the bounding model defined in Sec. 5.2.4 is also shown. (b) Comparison between σ_f values predicted by the covariance analysis versus Monte Carlo simulations for the two trajectories.

than those of the bounding model. In addition, the value of σ_f for the two reference trajectories is almost identical for all cruise durations. In Sec. 5, it is shown that $\boldsymbol{\rho}(t)$ does not have a significant effect on the error dynamics. This finding is consistent with Fig. 7(a), in which the only difference between the longitudinal and lateral retargeting maneuvers is the evolution of $\boldsymbol{\rho}(t)$ during the cruise.

These covariance propagation predictions were also verified by running 5000 Monte Carlo simulations for each trajectory. These simulations use the high-fidelity nonlinear solver described in Sec. 3.4 to propagate the telescope and starshade absolute positions. In the inset of Fig. 2, the cloud of $\delta\boldsymbol{\rho}_f$ vectors computed with Monte Carlo simulations for lateral retargeting is compared with the 3σ retargeting error ellipsoid predicted by the covariance analysis. The value of $\delta\rho_f$ as a function of t_f is shown for a subset of the longitudinal-retargeting-trajectory simulations in Fig. 7(a). The difference between the σ_f value predicted by the covariance analysis and the σ_f value computed from the Monte Carlo sample covariance matrix is shown in Fig. 7(b) for the two trajectories. It is found to remain within 3% for all t_f values in both cases.

Based on these results, a CS FOV of ±1.17° and ±0.66° would be required to guarantee successful reacquisition at a $3\sigma_f$ level at the end of the longitudinal and lateral retargeting cruises, respectively. As mentioned in Sec. 4.1, however, the conservative combinations of anisotropic sources of uncertainty were considered in the analysis, and the choice of nominal parameters and trajectories do not conform to a specific DRM. For instance, no longitudinal retargeting maneuvers are expected in the Starshade Rendezvous Probe study (Ref. 9). Nonetheless, the results presented here show that a CS with an FOV under 2° would be sufficient to enable successful retargeting even with these conservative assumptions.

4.5 *Application to HabEx-Starshade Scenario*

Going further, the covariance propagation framework is applied to a HabEx-starshade scenario, using the bounding model from Sec. 5.2.4 for simplicity. As HabEx would also be flying in a quasi-halo orbit near SEL2, the Roman nominal trajectory is maintained. Based on Ref. 11, the nominal telescope–starshade distance is increased to 76 Mm. A retargeting cruise duration of 30 days is considered. The starshade SRP uncertainty is increased by a factor of 4 to reflect the fact that the HabEx starshade would have a 52-m diameter rather than a 26-m diameter. HabEx retargeting burns are also larger, and a bounding value of 100 m/s is considered. For a mass of 5230 kg and a main thruster force of 445 N, the analysis in Appendix A predicts an execution error standard deviation of 0.142 m/s.

With these parameters, the predicted $3\sigma_f$ value is 3195 km or 2.41°. This preliminary assessment shows that even for a HabEx-starshade scenario, the proposed retargeting architecture is feasible with a degree-level CS FOV.

5 Sensitivity Analysis

In this section, the retargeting performance is analyzed with simpler models of the error dynamics. The purpose is to understand analytically the contributions of both nominal parameters and sources of uncertainty to the overall retargeting error. To do so, time-invariant models of the error dynamics are constructed with increasing complexity: no gravity-gradients, constant Earth-only gradient, and constant Earth-Moon-Sun gradients. As discussed in Sec. 5.2.4, this last model, when combined with a worst-case selection of telescope and starshade positions, produces a bounding, time-invariant model that provides significant insight into the retargeting error drivers. These models and their error predictions for a representative scenario are summarized in Table 4.

5.1 *Retargeting Error with No Gravity Gradient*

Gravity gradients at SEL2 are significantly shallower than in low Earth orbit. The double-integrator model below is therefore examined to quantify the effect of gravity gradients on the retargeting error. Denoting variables associated with this gravity-gradient-free model with an overbar, the state matrix simplifies to

$$\bar{A} = \begin{bmatrix} 0 & I & 0 \\ 0 & 0 & I \\ 0 & 0 & 0 \end{bmatrix}, \tag{18}$$

and the relative position error dynamics simplify to

$$\delta\bar{\boldsymbol{\rho}}_f = \delta\boldsymbol{\rho}_0 + +\delta\dot{\boldsymbol{\rho}}_0 t_f + \sum_{i=1}^{n} [t_f - (i-1)\Delta t_{\mathrm{desat}}]\delta\dot{\boldsymbol{r}}_{\mathrm{desat},i} + \frac{1}{2}\delta\ddot{\boldsymbol{\rho}}_{\mathrm{SRP}} t_f^2, \tag{19}$$

where $\delta\dot{\boldsymbol{r}}_{\mathrm{desat},i}$ is the i'th desat residual impulse vector. The system dynamics are time invariant and uncoupled from the telescope absolute dynamics. These equations are also isotropic: errors grow at the same rate in all directions. The final relative position error is evaluated analytically as

$$\bar{\sigma}_f^2 = \sigma_{\delta\rho,0}^2 + \sigma_{\delta\dot{\rho},0}^2 t_f^2 + \sum_{i=1}^{n} [t_f - (i-1)\Delta t_{\mathrm{desat}}]^2 \sigma_{\delta\dot{r},\mathrm{desat}}^2 + \frac{1}{4}\sigma_{\delta\ddot{\rho},\mathrm{SRP}}^2 t_f^4. \tag{20}$$

Over 3 weeks, the position, velocity, desat, and SRP uncertainty contributions are 167 m, 95 km, 4 km, and 66 km to $\bar{\sigma}_f$, respectively. The total value of 116 km is therefore 20% smaller than the 145-km value corresponding with the full retargeting trajectories in Sec. 4.4.

Table 4 Summary of models. The σ_f values shown correspond to a 3-week cruise. For the first row, σ_f is approximately equal for the two retargeting trajectories. For the last two rows, $r_\oplus = 1{,}200$ Mm, $\rho = 37.7$ Mm, and $\theta_\oplus = 0°$ are considered.

Section	Key assumptions	Ψ_s	σ_f
Sec. 4.3	Time varying, linearized about full reference trajectories.	$\sum_{i=\oplus,\odot,☾}(-\mu_i/s_i^3)(I - 3\hat{\boldsymbol{s}}_i\hat{\boldsymbol{s}}_i^\dagger)$	145 km
Sec. 5.1	Time invariant, no gravity gradient.	0	116 km
Sec. 5.2.1	Time invariant, only Earth gravity gradient.	$(-\mu_\oplus/s_\oplus^3)(I - 3\hat{\boldsymbol{s}}_\oplus\hat{\boldsymbol{s}}_\oplus^\dagger)$	144 km
Sec. 5.2.4	Time invariant, Sun, Earth, Moon, telescope, starshade aligned.	$(\sum_{i=\oplus,\odot,☾} - \mu_i/s_i^3)(I - 3\hat{\boldsymbol{s}}_\oplus\hat{\boldsymbol{s}}_\oplus^\dagger)$	152 km

5.2 *Retargeting Error with Constant Gravity Gradient*

Next, in Sec. 5.2.1, the effect of Earth's gravity gradient is added for constant telescope and starshade positions. As a result, the model produces the instantaneous error growth due to Earth gravity for the assumed positions. Constant positions keep the model time invariant and thus amenable to analysis. Further, as discussed in Ref. 12, Earth is the dominant influence on formation flying dynamics at a telescope-Earth distance of 1200 Mm: it is about six times more significant than the Sun and over 20 times more significant than the Moon. As the relative dominance of Earth gravity decreases for larger Earth-telescope distances, the effects of the Sun and the Moon are also included in Sec. 5.2.4.

5.2.1 *Earth-gravity-only dynamical system*

Variables associated with the Earth-gravity-only constant position model, and to Earth in general, are denoted with the symbol $\oplus$. The model is constructed by replacing Ψ_s and Ψ_r in Eq. (4) with

$$\Psi_{\oplus s} = \frac{-\mu_\oplus}{s_\oplus^3}(I - 3\hat{\boldsymbol{s}}_\oplus \hat{\boldsymbol{s}}_\oplus^\dagger), \quad \Psi_{\oplus r} = \frac{-\mu_\oplus}{r_\oplus^3}(I - 3\hat{\boldsymbol{r}}_\oplus \hat{\boldsymbol{r}}_\oplus^\dagger), \tag{21}$$

where $\mu_\oplus$ is the Earth gravitational constant, $\boldsymbol{s}_\oplus$ is the Earth-starshade vector, and $\boldsymbol{r}_\oplus$ is the Earth-telescope vector. With no further loss of generality, the inertial frame is centered at Earth, and its first axis is aligned with the (constant) Earth-telescope vector: $\boldsymbol{r} = \boldsymbol{r}_\oplus = r_\oplus[1{,}0,0]^\dagger = r_\oplus \hat{\boldsymbol{r}}_\oplus$ and $\boldsymbol{s} = \boldsymbol{s}_\oplus = \boldsymbol{r}_\oplus + \boldsymbol{\rho}_\oplus = s_\oplus R_s[1{,}0,0]^\dagger = s_\oplus R_s \hat{\boldsymbol{r}}_\oplus$, where R_s is a rotation matrix. The final state is $\mathbf{x}_{\oplus f} = \Phi_{\oplus f}\boldsymbol{x}_0$, where $\Phi_{\oplus f} = \exp(A_\oplus t_f)$ and $A_\oplus$ is time invariant.

5.2.2 *Sensitivity to nominal trajectory parameters*

It can be shown that there does not exist a unique set of $\Psi_{\oplus s}$ and $\Psi_{\oplus r}$ matrices that maximizes $\sigma_{f,\oplus}$ for all P_0 matrices. Instead, contours of $\sigma_{f,\oplus}$ are shown in Fig. 8 as a function of nominal parameters and for the specific P_0 matrix defined above.

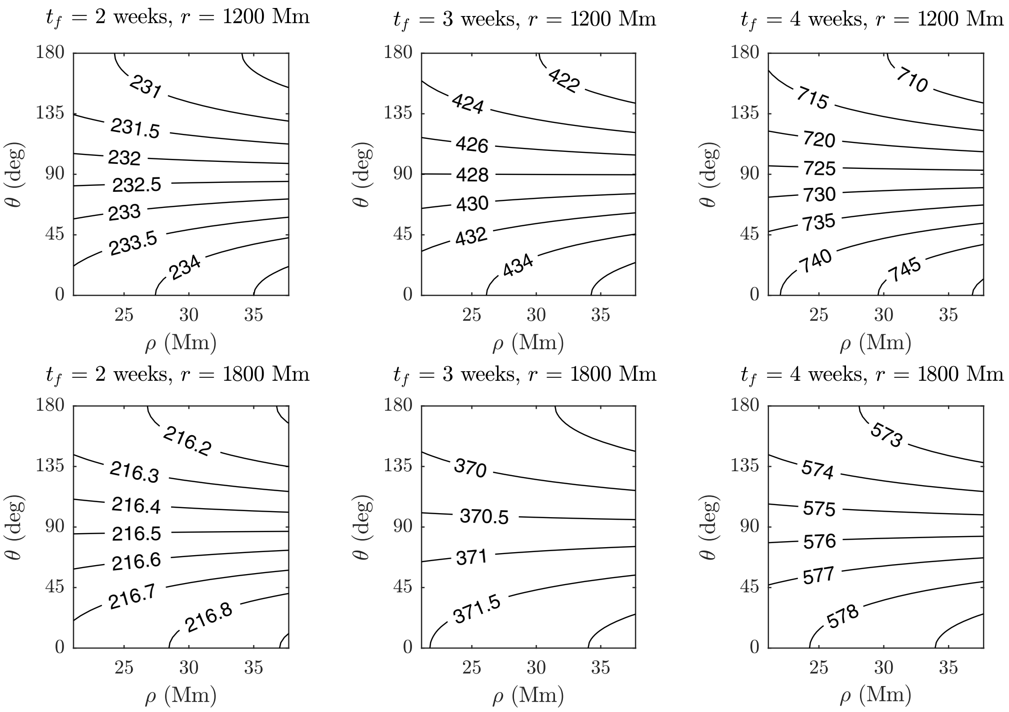

Fig. 8 Earth gravity-gradient model: contour plots of $3\sigma_{f,\oplus}$ in kilometers as a function of cruise duration t_f, nominal telescope distance to Earth $r_\oplus$, telescope-starshade nominal distance ρ, and Earth formation angle $\theta_\oplus$.

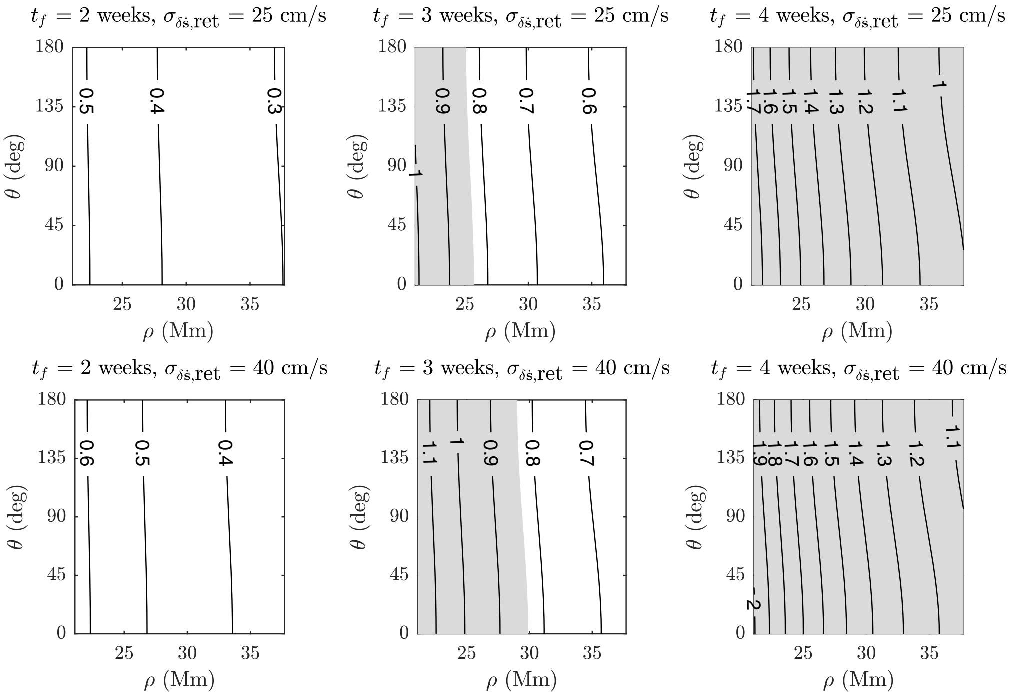

Fig. 9 Earth gravity-gradient model: contour plots of $3\sigma_{f,\oplus}$ retargeting angular error in degrees as a function of cruise duration t_f, nominal telescope distance to Earth $r_\oplus$, telescope-starshade nominal distance ρ, and Earth formation angle $\theta_\oplus$, for $r_\oplus = 1200$ Mm. As an example, regions exceeding a ±3000 arcsec (0.83°) CS FOV are grayed out.

Four observations are made in this paragraph and are revisited in Sec. 5.2.3. First, $\sigma_{f,\oplus}$ is maximized by small telescope–Earth distances $r_\oplus$. Second, $\sigma_{f,\oplus}$ is also maximized by small starshade–Earth distances $s_\oplus$, i.e., when $\theta_\oplus = 0°$ and ρ is maximized. Third, without gravity gradients, $3\overline{\sigma}_f = 210$, 348, and 520 km for $t_f = 2$, 3, and 4 weeks, respectively. Comparing these values to Fig. 8 shows that the influence of gravity gradients increases with t_f, especially for cruises longer than 2 weeks. Fourth, for given values of t_f and $r_\oplus$ (i.e., within a given contour plot in Fig. 8), $\sigma_{f,\oplus}$ changes by <6% for all combinations of $\theta_\oplus$ and ρ.

For reacquisition to be successful, the starshade must be in the FOV of the CS at $t = t_f$. In Fig. 9, the same results as in Fig. 8 are plotted in terms of the angular retargeting error rather than the relative position distance error. Although it was observed above that ρ only has a secondary influence on $\sigma_{f,\oplus}$, the size of the FOV in kilometers scales with ρ. As an example, Fig. 9 (bottom) predicts that reacquisition is not guaranteed at a $3\sigma_f$ confidence level with a CS FOV of ±3000 arcsec (0.83°) for cruises of 3 weeks if $\rho \lessapprox 30$ Mm. For cruises of 4 weeks, this FOV is not sufficient to guarantee reacquisition at any of the ρ values shown in the figure.

However, conservative uncertainty assumptions have been made as mentioned in Sec. 4.1. Moreover, in Figs. 8 and 9 (bottom), the value of $\sigma_{\delta\dot{s},\mathrm{ret}} = 40$ cm/s is kept constant. At close relative ranges, the starshade has to cover smaller distances for a given retargeting angle, so 3-week cruises with large retargeting burns are unlikely. Burns of smaller magnitude correspond to smaller execution errors, as discussed in Appendix A. Figure 9 (top) therefore shows the same results for $\sigma_{\delta\dot{s},\mathrm{ret}} = 25$ cm/s. In this case, the model predicts successful retargeting down to 26 Mm for 3-week cruises.

5.2.3 *State matrix modal decomposition*

To gain further insight into the system's dynamics, the eigendecomposition of the matrix $A_\oplus$ is evaluated analytically. The state matrix is $A_\oplus = \hat{U}_\oplus \Lambda_\oplus V_\oplus^\dagger$, and the final state transition matrix is $\Phi_{\oplus f} = \exp(A_\oplus t_f) = \hat{U}_\oplus \exp(\Lambda_\oplus t_f) V_\oplus^\dagger$. Here, $\hat{U}_\oplus$ is $A_\oplus$'s normalized eigenvector matrix (i.e., each eigenvector $\hat{\boldsymbol{u}}_i$ is normalized), $V_\oplus = (\hat{U}_\oplus^{-1})^\dagger$ is $A_\oplus$'s adjoint eigenvector matrix, and $\Lambda_\oplus$ is a diagonal matrix composed of $A_\oplus$'s eigenvalues. Before normalization, the eigenvector matrix can be shown to be

$$U_\oplus = \begin{bmatrix} R_s & R_s & R_s & -I & -I & -I \\ 0 & 0 & 0 & I & I & I \\ R_s\Lambda_s & -R_s\Lambda_s & 0 & -\Lambda_r & \Lambda_r & 0 \\ 0 & 0 & 0 & \Lambda_r & -\Lambda_r & 0 \\ 0 & 0 & -R_s\Lambda_s^2 & 0 & 0 & \Lambda_r^2 \\ 0 & 0 & 0 & 0 & 0 & -\Lambda_r^2 \end{bmatrix}, \tag{22}$$

where Λ_s and Λ_r are defined as

$$\Lambda_s = \mathrm{diag}(\lambda_{s1}, \quad \lambda_{s2}, \quad \lambda_{s3}) = \sqrt{\mu_\oplus/s_\oplus^3}\,\mathrm{diag}(\sqrt{2}, \quad \mathrm{j}, \quad \mathrm{j}), \tag{23}$$

$$\Lambda_r = \mathrm{diag}(\lambda_{r1}, \quad \lambda_{r2}, \quad \lambda_{r3}) = \sqrt{\mu_\oplus/r_\oplus^3}\,\mathrm{diag}(\sqrt{2}, \quad \mathrm{j}, \quad \mathrm{j}), \tag{24}$$

where $\mathrm{j} = \sqrt{-1}$ and $\mathrm{diag}(\cdot)$ is a diagonal matrix whose elements that are the arguments it operates on. The corresponding eigenvalue matrix can be shown to be

$$\Lambda_\oplus = \mathrm{diag}(\Lambda_s, \quad -\Lambda_s, \quad 0, \quad \Lambda_r, \quad -\Lambda_r, \quad 0). \tag{25}$$

In Eq. (22), the first, second, and third pairs of rows represent position, velocity, and acceleration components respectively, like the state vector in Eq. (3). The left three columns only have nonzero relative error components. Therefore, they correspond to pure starshade error dynamics. The right three columns only have equal-and-opposite absolute telescope error components and relative error components. Therefore, they correspond to pure telescope error dynamics.

In general, the angle between $\boldsymbol{s}_\oplus$ and $\boldsymbol{r}_\oplus$ is small because $\rho \ll r_\oplus$. If $R_s = I$ holds exactly, Eq. (22) shows that the dynamics along and across the $\boldsymbol{r}_\oplus$ axis are entirely decoupled because Λ_s and Λ_r are diagonal matrices.

Four of $A_\oplus$'s eigenvalues are the real stable–unstable pairs $\pm\lambda_{s1}$ and $\pm\lambda_{r1}$. The unstable eigenvalues λ_{s1} and λ_{r1} are maximized by minimizing $r_\oplus$ and $s_\oplus$, consistent with the first and second observations from Sec. 5.2.2 respectively. The two pairs of associated eigenvectors in Eq. (22) show that these modes correspond to error growth and decay along $\boldsymbol{r}_\oplus$ and $\boldsymbol{s}_\oplus$, i.e., the Earth-spacecraft directions. As an example, if $r_\oplus = 1{,}200$ Mm, $\rho = 37.7$ Mm, and $\theta_\oplus = 0°$ (so that $R_s = I$), growth/decay time constants are 16.2 and 17.0 days. These values are consistent with the third observation from Sec. 5.2.2.

Next, $A_\oplus$ has four pairs of purely imaginary complex-conjugate eigenvalues: $\pm\lambda_{s2} = \pm\lambda_{s3}$ and $\pm\lambda_{r2} = \pm\lambda_{r3}$. The four pairs of associated eigenvectors in Eq. (22) show that these modes correspond to constant amplitude oscillations in the two axes normal to $\boldsymbol{r}_\oplus$ and the two axes normal to $\boldsymbol{s}_\oplus$, respectively. With the same parameters as above, the periods of the oscillations are 144.3 and 151.4 days, i.e., much longer than the retargeting cruise duration.

The final six eigenvalues have a zero growth rate. Physically, they represent the shift of the system's equilibrium state, away from $\boldsymbol{x}_0 = \boldsymbol{0}$, caused by SRP uncertainty. The system is at its equilibrium when the starshade and telescope true positions are such that the gravity gradient acceleration is exactly canceled by the SRP uncertainty acceleration.

Out of these 18 modes, the only 6 that depend on $\boldsymbol{\rho}$ are $\pm\lambda_{si}$ for $1 \leqslant i \leqslant 3$. Equation (23) shows that these eigenvalues scale with $s_\oplus^{-3/2} \approx r_\oplus^{-3/2}[1 - (3/2)(\rho/r_\oplus)\cos(\theta_\oplus)]$. Therefore, as $\theta_\oplus \to 90°$, the distance ρ is expected to have a vanishing impact on the dynamical system, as confirmed by the horizontal contour lines near $\theta_\oplus = 90°$ in Fig. 8. For Roman-starshade parameters, the effect of ρ is maximized when $\rho = 37.7$ Mm, $r_\oplus = 1{,}200$ Mm, and $\theta_\oplus = 0°$, which leads to $(3/2)(\rho/r_\oplus)\cos(\theta_\oplus) = 0.047$. Therefore, the fourth observation from Sec. 5.2.2 is explained by the fact that the choice of $\boldsymbol{\rho}$ cannot change any of $A_\oplus$'s eigenvalues by more than 5%.

Although the modal decomposition above explains the trends observed in Sec. 5.2.2, it is not sufficient to fully understand the system's dynamics. For Roman-starshade parameters, the growth of the relative position error over 4 weeks due to individual eigenmodes can be no larger than a factor of $\exp(\lambda_{s1} t_f) \approx 5.6$. By contrast, recalling that $\sigma_{\delta\rho,\mathrm{sci}} = 167$ m, Fig. 8 shows that the largest growth factor is actually ~1500. This discrepancy between modal and transient growth is explained by non-normality in the system (e.g., Ref. 44): the initial state leading to the worst-case retargeting error σ_f has components along several nonorthogonal eigenvectors that have different growth/decay rates. As a result, the output norm can temporarily grow faster than if the initial state were aligned with any individual unstable mode.

Although the covariance analysis framework introduced above does output the worst-case transient output norm σ_f, its value alone does not provide insights into the mechanisms through which the retargeting error grows. To address this limitation, Appendix B shows how to compute the unique set of appropriately scaled initial conditions and disturbances (i.e., desats), collected in the vector $\tilde{z}_0$, that lead to the worst-case output norm σ_f for given P_0 and Q_k matrices. The "angle" between two systems' $\tilde{z}_0$ vectors therefore provides a measure of how similar the error growth mechanisms leading to σ_f are for the two systems, as illustrated in the next section.

5.2.4 *Bounding model*

Sections 5.2.2 and 5.2.3 show that $\theta_\oplus$ only has a secondary influence on the error dynamics and that $\theta_\oplus = 0°$ maximizes $\sigma_{f,\oplus}$. If $\theta_\oplus = 0°$ and the Sun and Moon are in line with the Earth, starshade, and telescope, then $\hat{\boldsymbol{s}}_\oplus = \hat{\boldsymbol{s}}_\odot = \hat{\boldsymbol{s}}_☾ = \hat{\boldsymbol{r}}_\oplus = \hat{\boldsymbol{r}}_\odot = \hat{\boldsymbol{r}}_☾$, where $\odot$ refers to the Sun and ☾ refers to the Moon. As a result, the linear system in Eq. (21) is unmodified, except that

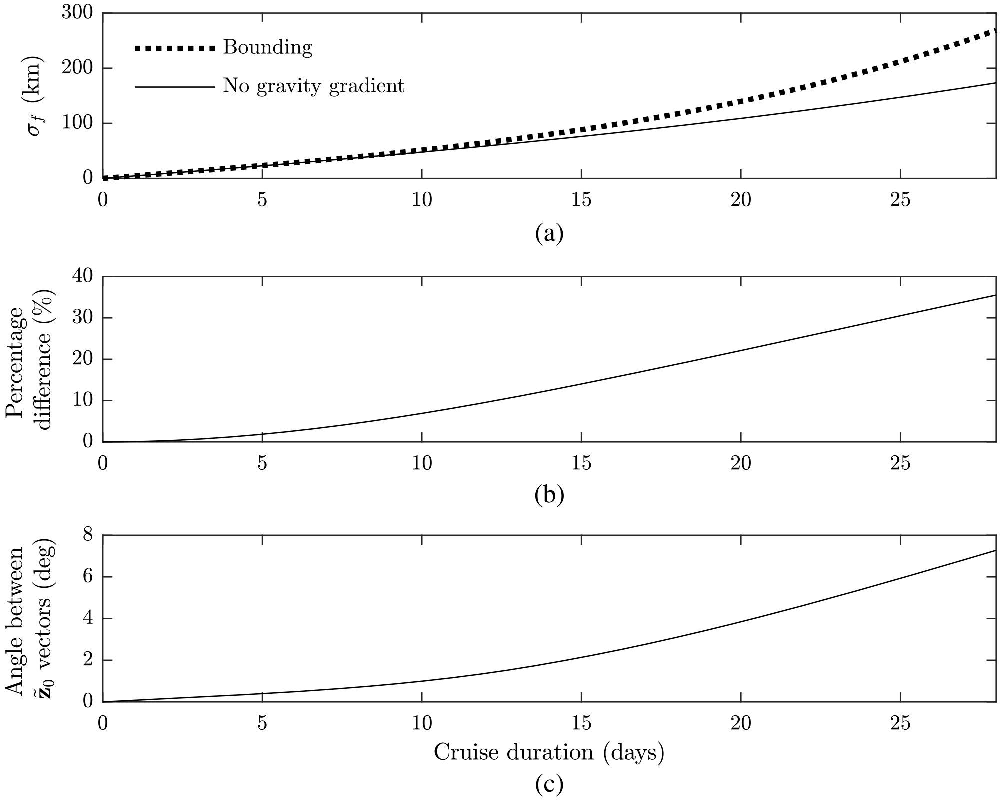

Fig. 10 Comparison of the worst-case growth of relative position error through the bounding model and gravity-gradient-free model. (a) σ_f as a function of cruise time t_f. (b) Percentage error between σ_f values, relative to bounding model. (c) Angle between the initial conditions and disturbances vectors $\tilde{\boldsymbol{z}}_0$ corresponding to σ_f for the two systems (see Appendix B).

$\mu_\oplus/r_\oplus^3$ becomes $(\mu_\oplus/r_\oplus^3+\mu_\odot/r_\odot^3+\mu_\leftmoon/r_\leftmoon^3)$ and $\mu_\oplus/s_\oplus^3$ becomes $(\mu_\oplus/s_\oplus^3+\mu_\odot/s_\odot^3+\mu_\leftmoon/s_\leftmoon^3)$, as summarized in Table 4. Using the findings from Sec. 5.2.2, if the largest representative value of ρ and the smallest representative values of $r_\oplus$, $r_\odot$, and $r_\leftmoon$ are used, this system is expected to lead to bounding transient growth for all cruise durations.

This bounding model with $r_\oplus = 1{,}200$ Mm, $\theta_\oplus = 0°$, and $\rho = 37.7$ Mm is compared with the gravity-gradient-free model in Fig. 10. While the gravity-gradient-free model is a decoupled isotropic double integrator, the bounding model is an unstable model where relative and absolute error dynamics are coupled and grow anisotropically. Thus, when $t_f = 4$ weeks, the final relative position error 1σ covariance ellipsoid is a 173-km-radius sphere for the gravity-gradient-free model. By contrast, the ellipsoid dimensions are 269, 137, and 137 km for the bounding model: without gravity gradients, the retargeting error is 36% smaller along the Earth-telescope axis but 26% larger in the directions normal to it.

Despite these differences, the angle between the two corresponding $\tilde{z}_0$ vectors is only 7.3° [see Fig. 10(c)]. This similarity shows that, although gravity gradients do measurably increase σ_f for

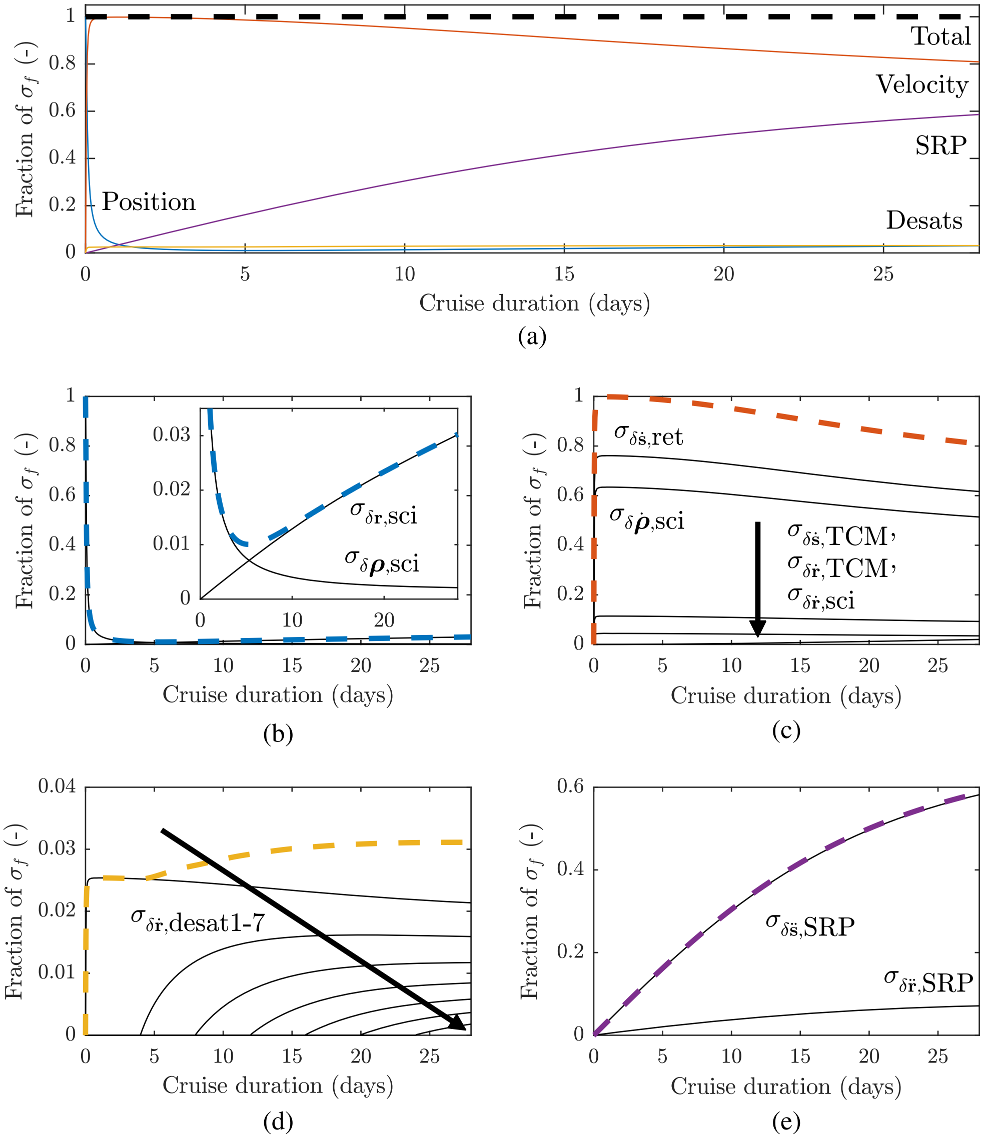

Fig. 11 (a) Normalized contribution to σ_f from each source of uncertainty. Components are shown for (b) initial position uncertainty (the inset is a close-up of small contributions), (c) initial velocity uncertainty, (d) desat uncertainty, and (e) SRP uncertainty.

cruise durations between 2 and 4 weeks, their influence is not sufficient to fundamentally change the distribution of initial conditions and disturbances that maximize it. Due to the relatively benign environment at SEL2, it takes longer cruises for the unstable modes associated with gravity gradients to dominate the dynamics. As an example, consider a cruise duration of 100 days, when t_f is 6.5 and 6.8 times as large as the two unstable mode time constants in the bounding system. In this case, the angle between the $\tilde{z}_0$ vector of the bounding and the gravity-gradient-free system is 29.8°, indicating that different error growth mechanisms are involved. Thus, during Roman-starshade retargeting cruises, σ_f mostly grows through a double-integrator-like propagation of initial errors and disturbances, which is further exacerbated by gravity gradients.

5.2.5 *Sensitivity to sources of uncertainty*

In this section, the sensitivity of σ_f to the sources of uncertainty included in the analysis is evaluated. Appendix C shows that σ_f can be formulated as the root-sum-square (RSS) of contributions due to each source of uncertainty, including desats. With this formulation, all of the contributions of σ_f can be evaluated with a single covariance propagation simulation. The relative importance of the different contributions as a function of t_f is shown in Fig. 11 for the bounding model. The distribution of contributions after 3 weeks is also shown in Fig. 12(a).

The value of σ_f is dominated by the initial relative position error for very short cruise durations. As t_f increases beyond a few hours, the velocity errors begin to dominate. In particular, the retargeting burn execution error is the largest contributor, followed by the initial relative velocity knowledge uncertainty from the science phase. Figure 11 also shows the influence of desat residuals: the later the maneuver is triggered during the cruise, the less time its residuals have to grow. Finally, for t_f values beyond a week, the influence of the relative position SRP uncertainty becomes considerable. For a cruise time of 3 weeks and beyond, it becomes one of the dominant contributors to the retargeting error. For all t_f values, as expected, $\sigma_{\delta r,\text{sci}}$ and $\sigma_{\delta \dot{r},\text{sci}}$ each contribute <5% of the total error.

In Appendix C, it is also shown that the normalized sensitivity of σ_f to small fractional changes in individual sources of uncertainty can be expressed as the square of the corresponding normalized contribution. Figure 12(b) shows these sensitivities after a cruise of 3 weeks. It illustrates that σ_f is highly sensitive to small fractional changes in its larger contributors but is almost not sensitive at all to changes in nondominant contributors. In this case, it shows that efforts to reduce σ_f are likely to be most effective if they focus on reducing $\sigma_{\delta\dot{\rho},\text{sci}}$, $\sigma_{\delta\dot{s},\text{ret}}$, and $\sigma_{\delta\ddot{s},\text{SRP}}$.

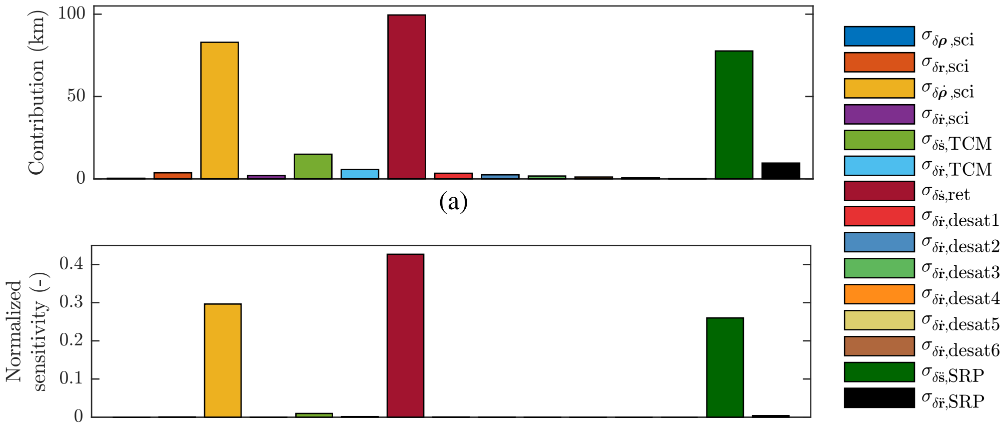

(b)

Fig. 12 (a) Absolute contributions to σ_f at $t_f = 3$ weeks. (b) Normalized sensitivities of σ_f at $t_f = 3$ weeks.

6 Conclusions

In this article, a retargeting architecture for a starshade flying in formation with a space telescope at Sun–Earth L2 (SEL2) is proposed and shown to be feasible. Over several weeks, the starshade travels tens of thousands of kilometers to align itself with the telescope's next target star. It must do so with sufficient precision to be reacquired by the telescope's dedicated coarse acquisition sensor (CS), which has a degree-level FOV.

The proposed retargeting architecture uses chemical propellant only and does not require intermittent starshade position measurements either from the ground or the telescope. It hinges on the use of an array of COTS accelerometers on board the starshade spacecraft that drive down the retargeting burn execution error to a level that enables reacquisition with the CS. It is hoped that this architecture could reduce the cost and complexity of prospective starshade missions.

The feasibility of the architecture is demonstrated through a verified covariance analysis framework. A CS FOV under 2° is found to be sufficient for reacquisition after 3 week retargeting maneuvers for a Roman-starshade scenario. An FOV under 3° is also found to be sufficient for a HabEx-starshade scenario.

Further analysis shows that the relative position errors grow mostly through the propagation of initial state uncertainty and disturbances, which are exacerbated by SEL2 gravity gradients. With the parameter values considered in the analysis, the retargeting burn execution error, science phase relative velocity uncertainty, and starshade SRP uncertainty are found to be the largest contributors. For cruise durations beyond about 2 weeks, gravity gradients significantly increase the worst-case retargeting error. This effect is sensitive to the absolute distance between the two spacecraft and Earth. The relative position between the telescope and the starshade, however, only has a secondary influence. Overall, as might be expected, the combination of large burns, long cruise durations, and short final reacquisition ranges is most stressing to this retargeting architecture.

Having developed a framework that accurately evaluates starshade retargeting error statistics and sensitivities, the next step to be addressed in future work is to apply this tool to specific starshade DRMs and generate tailored estimates of expected retargeting performance.

7 Appendix A: Retargeting Burn Execution Error

In this appendix, the retargeting burn execution error statistics are evaluated as a function of relevant sources of uncertainty. The model is then applied to the proposed retargeting ConOps with Roman-starshade parameters.

7.1 *Burn Execution Error*

In this section, an expression for ${}^{\mathcal{I}}\delta\Delta\boldsymbol{v}_{\text{exec}}$, the inertial frame execution error due to a Δv performed by the starshade's main thrusters, is derived:

$$
{}^{\mathcal{I}}\delta\Delta\boldsymbol{v}_{\text{exec}} = {}^{\mathcal{I}}\Delta\boldsymbol{v}^{*} - {}^{\mathcal{I}}\Delta\boldsymbol{v}, \tag{26}
$$

where $\mathcal{I}$ denotes the inertial frame quantities and ${}^{\mathcal{I}}\Delta\boldsymbol{v}^{*}$ and ${}^{\mathcal{I}}\Delta\boldsymbol{v}$ are the true and nominal (i.e., commanded) Δv vectors, respectively. Without loss of generality, the inertial frame is defined as having its third axis aligned with the commanded burn direction: ${}^{\mathcal{I}}\Delta\boldsymbol{v} = [0,0,1]^{\dagger}$.

First, an accelerometer error model is introduced, and the corresponding error vector in individual measurements is derived. The first-order effects of accelerometer noise, bias, scale factor errors, internal misalignments, known mounting misalignment, and mounting misalignment uncertainty are taken into account. Spacecraft pointing errors and spacecraft pointing uncertainty are also included.

Second, an expression for the full execution error vector ${}^{\mathcal{I}}\Delta\boldsymbol{v}_{\text{exec}}$ is derived based on this accelerometer model. As described in Sec. 2.1, the retargeting Δv is performed with the starshade main thrusters, nominally aligned with the commanded burn direction. The RCS thrusters are used to control attitude during the burn, closing the loop on measurements from a set of accelerometers to reduce the execution error. The burn is terminated when the total estimated Δv vector matches the commanded Δv vector up to a given threshold.

7.1.1 *Accelerometer model*

The accelerometer outputs incremental Δv measurements at fixed time intervals Δt. The time since the start of the burn is $t = k\Delta t$. The error in the k'th measurement is

$$ {}^{\mathcal{I}}\delta\Delta\boldsymbol{v}_{\text{meas},k} = {}^{\mathcal{I}}\Delta\boldsymbol{v}_{\text{meas},k} - {}^{\mathcal{I}}\Delta\boldsymbol{v}_k^*, \tag{27} $$

where ${}^{\mathcal{I}}\Delta\boldsymbol{v}_{\text{meas},k}$ and ${}^{\mathcal{I}}\Delta\boldsymbol{v}_k^*$ are the measured and true Δv increment vectors, respectively.

The accelerometer model derived in Ref. 45 is used to compute the error in terms of the accelerometer parameters. Markov bias, high-order bias coefficients, and all second-order error terms are considered negligible. Gravity gradient and SRP accelerations are also considered negligible compared with the acceleration due to thrusters. The resulting model is

$$ {}^{\mathcal{A}}\Delta\boldsymbol{v}_{\text{meas},k} = (I + {}^{\mathcal{A}}M){}^{\mathcal{A}}\Delta\boldsymbol{v}_k^* + {}^{\mathcal{A}}\Delta\boldsymbol{v}_{\delta,k}, \tag{28} $$

$$ {}^{\mathcal{A}}M = {}^{\mathcal{A}}N_{\text{int}} + {}^{\mathcal{A}}K, \quad {}^{\mathcal{A}}\Delta\boldsymbol{v}_{\delta,k} = {}^{\mathcal{A}}\boldsymbol{n}_k + {}^{\mathcal{A}}\boldsymbol{b}, \tag{29} $$

where $\mathcal{A}$ denotes the accelerometer-frame quantities, ${}^{\mathcal{A}}N_{\text{int}}$ is the internal accelerometer misalignment matrix, ${}^{\mathcal{A}}K$ is the diagonal matrix of accelerometer scale factors along the accelerometer axes (assumed to span an orthogonal right-handed set), ${}^{\mathcal{A}}\boldsymbol{n}_k$ is the accelerometer noise vector, and ${}^{\mathcal{A}}\boldsymbol{b}$ is the accelerometer bias vector. Individual components of these four sources of uncertainty are uncorrelated and zero-mean normally distributed random variables. The associated component standard deviations are σ_{int}, σ_K, σ_n, and σ_b, respectively.

In practice, the accelerometers are often provided as a set of four single-axis units laid out in a pyramidal configuration, which provides some averaging and redundancy. The assumption that there are three orthogonal single-axis accelerometers is thus conservative.

7.1.2 *Accelerometer measurement error*

The following expression for the inertial frame incremental measurement error can be derived:

$$ {}^{\mathcal{I}}\delta\Delta\boldsymbol{v}_{\text{meas},k} = {}^{\mathcal{I}}M_{\text{tot},k}{}^{\mathcal{I}}\Delta\boldsymbol{v}_k^* + {}^{\mathcal{I}}\Delta\boldsymbol{v}_{\delta,k}, \tag{30} $$

$$ {}^{\mathcal{I}}M_{\text{tot},k} = R^{\mathcal{IB}}({}^{\mathcal{B}}N_{n,k}^{\mathcal{IB}} + {}^{\mathcal{B}}N_b^{\mathcal{IB}})R^{\mathcal{BI}} + R^{\mathcal{IA}}({}^{\mathcal{A}}N^{\mathcal{BA}} + {}^{\mathcal{A}}N_{\text{int}} + {}^{\mathcal{A}}K)R^{\mathcal{AI}}, \tag{31} $$

$$ {}^{\mathcal{I}}\Delta\boldsymbol{v}_{\delta,k} = R^{\mathcal{IA}}({}^{\mathcal{A}}\boldsymbol{n}_k + {}^{\mathcal{A}}\boldsymbol{b}), \tag{32} $$

where $\mathcal{B}$ denotes the body-frame quantities. Rotation matrices are denoted, for example, by $R^{\mathcal{IA}}$, which is the accelerometer frame to inertial frame rotation matrix. In the equation above, ${}^{\mathcal{B}}N_{n,k}^{\mathcal{IB}}$, ${}^{\mathcal{B}}N_b^{\mathcal{IB}}$, and ${}^{\mathcal{A}}N^{\mathcal{BA}}$ are the pointing knowledge noise, pointing knowledge bias, and mounting misalignment uncertainty contributions, respectively. The three distinct components of each matrix are uncorrelated and zero-mean normally distributed random variables, with standard deviations of $\sigma_{n,\mathcal{IB}}$, $\sigma_{b,\mathcal{IB}}$, and $\sigma_{\mathcal{BA}}$, respectively. In addition, it can be shown that the effect of zero-mean but known pointing control error and known accelerometer mounting misalignments cancel to first order.

7.1.3 Δv *Execution error*

In this section, an expression for the full Δv execution error vector is derived based on the accelerometer model introduced above. Whereas the commanded burn ${}^{\mathcal{I}}\Delta\boldsymbol{v}$ is known on board, ${}^{\mathcal{I}}\Delta\boldsymbol{v}^*$, the final true realized impulse, is a stochastic vector that depends on how the on-board system controls the burn execution and termination. An explicit expression for ${}^{\mathcal{I}}\Delta\boldsymbol{v}^*$ is thus derived in terms of known quantities and sources of uncertainty with known statistics using the expression for ${}^{\mathcal{I}}\delta\Delta\boldsymbol{v}_{\text{meas},k}$ derived above.

When the burn is stopped, at the final time step $k = n_k$, the integrated accelerometer measurement is

$$ {}^{\mathcal{I}}\Delta\boldsymbol{v}_{\text{meas}} = \sum_{k=1}^{n_k} {}^{\mathcal{I}}\Delta\boldsymbol{v}_{\text{meas},k} = {}^{\mathcal{I}}\Delta\boldsymbol{v} + {}^{\mathcal{I}}\Delta\boldsymbol{v}_{\text{ctl}}, \tag{33} $$

where ${}^{\mathcal{I}}\Delta\boldsymbol{v}_{\text{ctl}}$ is the measured but uncorrected control error at burn termination. Its statistics are known and depend on both the nominal burn itself and the selected burn termination criteria, discussed in Sec. 7.2.3. With this definition, the execution error can be shown to be

$$ {}^{\mathcal{I}}\delta\Delta\boldsymbol{v}_{\text{exec}} = \left(-\frac{1}{n_k}\sum_{k=1}^{n_k} {}^{\mathcal{I}}M_{\text{tot},k}\right) {}^{\mathcal{I}}\Delta\boldsymbol{v} - \sum_{k=1}^{n_k} {}^{\mathcal{I}}\Delta\boldsymbol{v}_{\delta,k} + {}^{\mathcal{I}}\Delta\boldsymbol{v}_{\text{ctl}}. \tag{34} $$

7.1.4 *Averaging multiple accelerometers*

The measurement from n_{acc} three-axis accelerometers is computed on board and averaged to find the final acceleration measurement. The sources of uncertainty are zero-mean normally distributed random variables that depend on the accelerometer model. As a result, when several accelerometers are used, each one has different error characteristics. However, all accelerometers are subject to the same pointing knowledge error. If all accelerometers are nominally coaligned, the averaged execution error can be shown to be

$$ {}^{\mathcal{I}}\delta\Delta\boldsymbol{v}_{\text{exec,avg}} = \left(\frac{-1}{n_{\text{acc}}}\sum_{i=1}^{n_{\text{acc}}} \frac{1}{n_k}\sum_{k=1}^{n_k} {}^{\mathcal{I}}M_{\text{tot},k,i}\right) {}^{\mathcal{I}}\Delta\boldsymbol{v} + \frac{-1}{n_{\text{acc}}}\sum_{i=1}^{n_{\text{acc}}}\sum_{k=1}^{n_k} {}^{\mathcal{I}}\Delta\boldsymbol{v}_{\delta,k,i} + {}^{\mathcal{I}}\Delta\boldsymbol{v}_{\text{ctl}}, \tag{35} $$

where the known control error does not benefit from accelerometer averaging. Rather, it is a function of the RCS control loop, as discussed in Sec. 7.2.3.

7.2 *Burn Execution Error Statistics*

7.2.1 *Execution error covariance matrix*

The execution error expectation $E({}^{\mathcal{I}}\delta\Delta\boldsymbol{v}_{\text{exec,avg}})$ is zero as it is a linear combination of uncorrelated zero-mean random variables. Its covariance matrix $P_{\text{exec}} = \text{Cov}({}^{\mathcal{I}}\delta\Delta\boldsymbol{v}_{\text{exec,avg}})$ is

$$ P_{\text{exec}} = R^{\mathcal{IB}}(P_{n,\mathcal{IB}} + P_{b,\mathcal{IB}})R^{\mathcal{BI}} + R^{\mathcal{IA}}(P_{\mathcal{BA}} + P_{\text{int}} + P_K)R^{\mathcal{AI}} + P_\delta + P_{\text{ctl}}, \tag{36} $$

$$ P_{n,\mathcal{IB}} = \frac{-1}{n_k}\text{Cov}[{}^{\mathcal{B}}N_{n,k}^{\mathcal{IB}}({}^{\mathcal{B}}\Delta\boldsymbol{v})], \quad P_{b,\mathcal{IB}} = -\text{Cov}[{}^{\mathcal{B}}N_b^{\mathcal{IB}}({}^{\mathcal{B}}\Delta\boldsymbol{v})], \tag{37} $$

$$ P_{\mathcal{BA}} = \frac{-1}{n_{\text{acc}}}\text{Cov}[{}^{\mathcal{A}}N^{\mathcal{BA}}({}^{\mathcal{A}}\Delta\boldsymbol{v})], \tag{38} $$

$$ P_{\text{int}} = \frac{-1}{n_{\text{acc}}}\text{Cov}[{}^{\mathcal{A}}N_{\text{int}}({}^{\mathcal{A}}\Delta\boldsymbol{v})], \tag{39} $$

$$ P_K = \frac{1}{n_{\text{acc}}}\text{Cov}[{}^{\mathcal{A}}K({}^{\mathcal{A}}\Delta\boldsymbol{v})], \tag{40} $$

where the statistics of each instance of ${}^{\mathcal{B}}N_{n,k}^{\mathcal{IB}}$, ${}^{\mathcal{B}}N_b^{\mathcal{IB}}$, ${}^{\mathcal{A}}N^{\mathcal{BA}}$, ${}^{\mathcal{A}}N_{\text{int}}$, and ${}^{\mathcal{A}}K$ are known and fixed both in time and across accelerometers.

7.2.2 *Open-loop execution error components*

The lateral and longitudinal open-loop execution errors are defined as the components of the error across and along the commanded burn direction, respectively. They are modeled as the sum of a fixed term and a proportional term:

$$\sigma^2_{\text{open,lat}} = \sigma^2_{\text{open,lat,fix}} + \Delta v^2_{\text{cmd}} \sigma^2_{\text{open,lat,prop}}, \quad \sigma^2_{\text{open,lon}} = \sigma^2_{\text{open,lon,fix}} + \Delta v^2_{\text{cmd}} \sigma^2_{\text{open,lon,prop}}, \tag{41}$$

where Δv_{cmd} is the commanded burn magnitude. As a result, the open-loop covariance matrix is $P_{\text{exec}} = \text{diag}(\sigma^2_{\text{open,lat}}, \sigma^2_{\text{open,lat}}, \sigma^2_{\text{open,lon}})$.

7.2.3 *Burn termination criteria*

Accelerometers and RCS thrusters are used to reduce the execution error from its open-loop value above to its closed-loop value given by Eq. (36). The covariance of this closed-loop execution error depends on the final control error term P_{ctl}.

In the longitudinal direction, the burn is terminated when the longitudinal impulse magnitude measured by the accelerometers is equal to Δv_{cmd}. Assuming timing biases have been calibrated out, the resulting longitudinal control error variance is

$$\sigma^2_{\text{ctl,lon}} = \frac{\Delta v^2_{\text{cmd}}}{t^2_{\text{burn}}} \sigma^2_{\text{timing}}, \tag{42}$$

where t_{burn} is the burn duration and σ_{timing} is the burn termination timing accuracy.

In the lateral directions, the RCS thrusters are used to close the loop on the main thruster's lateral execution errors, as measured with the accelerometers. This control loop is modeled by the sum of a fixed term and a residual that is a function of the control loop time constant t_{ctl}:

$$\sigma^2_{\text{ctl,lat}} = \sigma^2_{\text{ctl,lat,fix}} + \exp(-2t_{\text{burn}}/t_{\text{ctl}}) \sigma^2_{\text{open,lat}}. \tag{43}$$

If $t_{\text{burn}} \ll t_{\text{ctl}}$, the control loop is too slow to correct open-loop residuals and $\sigma^2_{\text{ctl,lat}}$ tends to $\sigma^2_{\text{ctl,lat,fix}} + \sigma^2_{\text{open,lat}}$. Conversely, if $t_{\text{burn}} \gg t_{\text{ctl}}$, the control loop is effective and $\sigma^2_{\text{ctl,lat}}$ tends to $\sigma^2_{\text{ctl,lat,fix}}$.

7.2.4 *Closed-loop execution error components*

Analytic expressions of the components of Eq. (36) are derived as follows. First, the burn termination criteria defined above are applied to the lateral and longitudinal components of P_{ctl}. Second, Eq. (36) is rewritten in terms of Δv_{cmd} and t_{burn} instead of n_k by expressing $\sigma_{n,\mathcal{IB}}$, $\sigma_{b,\mathcal{IB}}$, σ_n, and σ_b in terms of their continuous-time equivalents, denoted with an overbar. Third, P_K depends on the orientation of the accelerometer axes with respect to the nominal burn direction. It is diagonal if accelerometers axes are equidistant from the burn direction such that ${}^{\mathcal{A}}\Delta\boldsymbol{v} = [1,1,1]^{\dagger}(\Delta v_{\text{cmd}}/\sqrt{3})$. It is also diagonal if one axis is aligned with the burn such that $R^{\mathcal{IA}} = I$. In these two cases, the lateral and longitudinal components are expressed as

$$\begin{aligned}\sigma^2_{\text{exec,lat}} = {} & \left(\frac{\Delta v^2_{\text{cmd}}}{t_{\text{burn}}}\right)\bar{\sigma}^2_{n,\mathcal{IB}} + (\Delta v^2_{\text{cmd}})\bar{\sigma}^2_{b,\mathcal{IB}} + \left(\frac{\Delta v^2_{\text{cmd}}}{n_{\text{acc}}}\right)\sigma^2_{\mathcal{BA}} + \left(\frac{\Delta v^2_{\text{cmd}}}{n_{\text{acc}}}\right)\sigma^2_{\text{int}} \\ & + \left(\frac{\kappa_{\text{lat}}\Delta v^2_{\text{cmd}}}{n_{\text{acc}}}\right)\sigma^2_K + \left(\frac{t_{\text{burn}}}{n_{\text{acc}}}\right)\bar{\sigma}^2_n + \left(\frac{t^2_{\text{burn}}}{n_{\text{acc}}}\right)\bar{\sigma}^2_b + \sigma^2_{\text{ctl,lat}},\end{aligned} \tag{44}$$

$$\sigma^2_{\text{exec,lon}} = \left(\frac{\kappa_{\text{lon}}\Delta v^2_{\text{cmd}}}{n_{\text{acc}}}\right)\sigma^2_K + \left(\frac{t_{\text{burn}}}{n_{\text{acc}}}\right)\bar{\sigma}^2_n + \left(\frac{t^2_{\text{burn}}}{n_{\text{acc}}}\right)\bar{\sigma}^2_b + \sigma^2_{\text{ctl,lon}}, \tag{45}$$

where $\kappa_{\text{lat}} = \kappa_{\text{lon}} = 1/3$ in the equidistant case and $\kappa_{\text{lat}} = 0$ and $\kappa_{\text{lon}} = 1$ in the aligned case.

7.3 *Application to Roman-Starshade Scenario*

7.3.1 *Retargeting burn approach*

In this section, the execution error model derived above is applied to the Roman-starshade retargeting burn ConOps described in Sec. 2.1. The on-board accelerometers are used both during the main burn and during the two slews to measure residual Δvs (only while thrusters are firing). The total measured slew residual standard deviation is $\sigma_{\text{ctl,slew}}$ per axis. In addition, the measurement error of the slews is $\sigma^2_{\text{meas,slew}}$. The variances of the lateral and longitudinal components of the open-loop RCS correction burn are modeled as

$$\sigma^2_{\text{corr,lat}} = \sigma^2_{\text{corr,fix}} + (\sigma^2_{\text{ctl,slew}} + \sigma^2_{\text{ctl,lat}})\sigma^2_{\text{corr,prop}}, \quad \sigma^2_{\text{corr,lon}} = \sigma^2_{\text{corr,fix}} + (\sigma^2_{\text{ctl,slew}} + \sigma^2_{\text{ctl,lon}})\sigma^2_{\text{corr,prop}}. \tag{46}$$

After the correction burn is applied, the net execution error is evaluated by replacing $\sigma^2_{\text{ctl,lat}}$ and $\sigma^2_{\text{ctl,lon}}$ in Eq. (44) and Eq. (45) by $\sigma^2_{\text{corr,lat}}$ and $\sigma^2_{\text{corr,lon}}$, respectively, and adding in a further $\sigma^2_{\text{meas,slew}}$ contribution to each axis.

7.3.2 *Parameter selection*

A spacecraft mass of 1200 kg and four 22 N thrusters are considered. The performance of COTS and flight qualified sensors and actuators is assumed, as summarized in Tables 1, 2, and 5. In Table 5, the value of $\bar{\sigma}_b$ assumes that the accelerometer bias has been calibrated in flight before the retargeting burn takes place. One calibration strategy is to measure the SRP acceleration

Table 5 Uncertainty parameters for retargeting burn execution error.

Parameter	Symbol	Value (1σ/axis)
Internal misalignment	σ_{int}	1 mrad
Scale factor error	σ_K	100 ppm
Bias calibration residual	$\bar{\sigma}_b$	5 μm/s^2
Noise (10 Hz sampling)	$\bar{\sigma}_n$	$(7/\sqrt{10})$ μg/$\sqrt{\text{Hz}}$
Mounting alignment uncertainty	$\sigma_{\mathcal{BA}}$	2.62 mrad
Pointing knowledge uncertainty noise (10 Hz sampling)	$\bar{\sigma}_{n,\mathcal{IB}}$	$(2/\sqrt{10})$ arcsec/$\sqrt{\text{Hz}}$
Pointing knowledge uncertainty bias	$\sigma_{b,\mathcal{IB}}$	3 arcsec
Open-loop lateral burn residual proportional term	$\sigma_{\text{open,lat,prop}}$	2%
Open-loop lateral burn residual fixed term	$\sigma_{\text{open,lat,fix}}$	3.33 mm/s
Open-loop longitudinal burn residual proportional term	$\sigma_{\text{open,lon,prop}}$	2%
Open-loop longitudinal burn residual fixed term	$\sigma_{\text{open,lon,fix}}$	3.33 mm/s
Total control error from slew maneuvers	$\sigma_{\text{ctl,slew}}$	0.15 m/s
Total measurement error from slew maneuvers	$\sigma_{\text{meas.slew}}$	7.1 mm/s
Correction burn residual proportional term	$\sigma_{\text{corr,prop}}$	5%
Correction burn residual fixed term	$\sigma_{\text{corr,fix}}$	3.33 mm/s
Final closed-loop lateral control error fixed term	$\sigma_{\text{ctl,lat,fix}}$	3.33 mm/s
RCS control loop time constant	t_{ctl}	200 s
Burn termination timing accuracy	σ_{timing}	200 ms

acting on the precisely characterized 335 m^2 starshade surface area. Depending on the surface properties and propellant mass at the time of calibration, the SRP acceleration is expected to be at most 2.5 $\mu\mathrm{m/s}^2$. A conservative value of $\overline{\sigma}_b = 5\ \mu\mathrm{m/s}^2$ is thus used. The values of $\sigma_{\mathcal{BA}}$, σ_{open}, $\sigma_{\mathrm{ctl,lat,fix}}$, and t_{ctl} are consistent with flight projects such as Mars Science Laboratory and Europa Clipper. The value of $\sigma_{\mathrm{ctl,slew}}$ is based on the order-of-magnitude approximations for a burn performed with a technique similar to Ref. 46, and the value of $\sigma_{\mathrm{meas,slew}}$ was generated using the accelerometer model described in this section. In practice, for small burns, the model-based estimation of the execution error may be used if it is found to outperform accelerometer-based estimation.

7.3.3 *Results*

Figure 13 shows the execution error and its components as a function of the nominal burn magnitude for accelerometers axes that are equidistant from the burn direction. The lateral component of the error is larger than the longitudinal component, which is mostly due to the uncorrected control error, and remains approximately constant at about 21 mm/s. The largest contributions to the lateral execution error are the uncorrected control error after the correction burn and the accelerometer mounting and internal misalignments. For nominal burn magnitudes around 20 m/s, the total execution error standard deviation is below 40 cm/s. This value is therefore used in the covariance analysis above, unless specified otherwise.

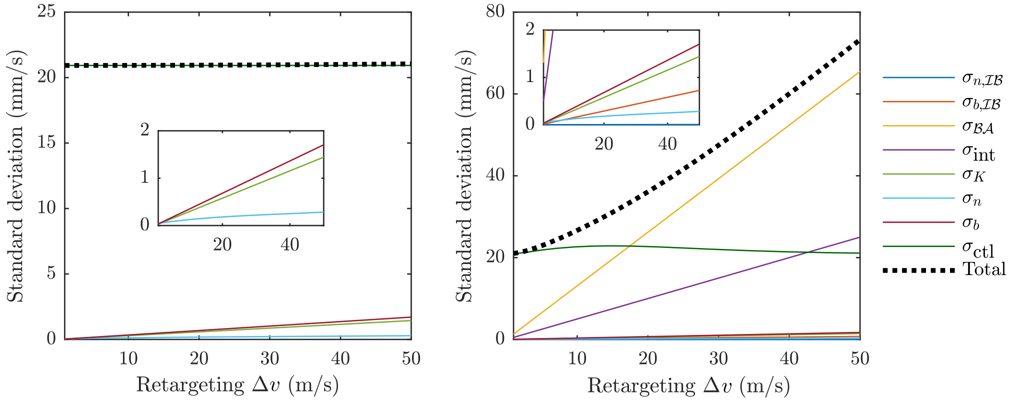

(a) (b)

Fig. 13 Contributions to (a) longitudinal and (b) lateral execution errors as a function of nominal burn magnitude. Insets show close-ups of small contributions.

8 Appendix B: Comparing Output Norms of LTI Systems

8.1 *LTI Systems Without Inputs*

In this section, a framework for comparing output norms of linear time-invariant (LTI) systems, regardless of diagonalizability and stability is introduced. The systems being compared must have no external inputs such that $\dot{\boldsymbol{x}} = A\boldsymbol{x}$. This assumption is relaxed in Sec. 8.2. They must also have the same state vector $\boldsymbol{x}$ and the same output matrix C, but potentially different state matrices A and initial state covariance matrices P_0.

The final output norm of such LTI systems is $\|\boldsymbol{y}_f\| = \|C\boldsymbol{x}_f\| = \|C\Phi_f\boldsymbol{x}_0\|$. It is common for individual states within $\boldsymbol{x}$ not to have the same units or nominal magnitudes (e.g., absolute versus relative position or position versus acceleration). For such systems, finding the initial state $\boldsymbol{x}_0$ that maximizes $\|\boldsymbol{y}_f\|$ while constraining the unweighted initial state norm $\|\boldsymbol{x}_0\| = \sqrt{\boldsymbol{x}_0^\dagger\boldsymbol{x}_0}$ may not be physically meaningful. Without a scaling matrix, this inner-product not only gives more weight to state variables with values that are naturally larger but may also sum quantities that have different physical units.

The inner-product can be made physically meaningful by changing the system coordinates using P_0. Using the initial covariance matrix, state variables can be expressed in terms of their likelihood. Here, the likelihood of a scalar initial state x_0 with standard deviation $\sigma_{x,0}$ is defined as $z_0 = x_0/\sigma_{x,0}$. In general, the initial state likelihood is given by $\sqrt{\boldsymbol{x}_0^\dagger P_0^{-1} \boldsymbol{x}_0} = \|P_0^{-1/2}\boldsymbol{x}_0\| = \|\boldsymbol{z}_0\|$. Here, $\boldsymbol{z_0} = P_0^{-1/2}\boldsymbol{x_0}$ is the initial state likelihood vector and $P_0^{-1/2}$ is found from the singular value decomposition (SVD) of the initial covariance matrix: $P_0 = \hat{U}_{P0}\Sigma_{P0}^2\hat{U}_{P0}^\dagger$. The following are then defined: $P_0^{-1/2} = \Sigma_{P0}^{-1}\hat{U}_{P0}^\dagger$ and $P_0^{1/2} = \hat{U}_{P0}\Sigma_{P0}$ so that $P_0^{1/2}P_0^{-1/2} = P_0^{-1/2}P_0^{1/2} = I$.

The transformed system dynamics are $\dot{\boldsymbol{z}} = A_z\boldsymbol{z}$, where $A_z = P_0^{-1/2}AP_0^{1/2}$ and the output $\boldsymbol{y} = CP_0^{1/2}\boldsymbol{z}$ is unchanged. In the transformed coordinates, the initial state covariance matrix is the identity matrix $E(\boldsymbol{z}_0\boldsymbol{z}_0^\dagger) = I$ and inner-products are now physically meaningful: $\|\boldsymbol{z}\|$ is the total likelihood of the state $\boldsymbol{x} = P_0^{1/2}\boldsymbol{z}$ and $\cos^{-1}[\boldsymbol{z}_1^\dagger\boldsymbol{z}_2/(\|\boldsymbol{z}_1\|\|\boldsymbol{z}_2\|)]$ is the "angle" between likelihood states $\boldsymbol{z}_1$ and $\boldsymbol{z}_2$.

Using this coordinate transformation, the initial state $\boldsymbol{x}_0$ that maximizes the final output norm $\|\boldsymbol{y}_f\|$, subject to $\|\boldsymbol{z}_0\| = 1$ is sought:

$$\|\boldsymbol{y}_f\|^2 = \boldsymbol{x}_0^\dagger\Phi_f^\dagger C^\dagger C\Phi_f\boldsymbol{x}_0 = \boldsymbol{z}_0^\dagger[(P_0^{1/2})^\dagger\Phi_f^\dagger C^\dagger C\Phi_f P_0^{1/2}]\boldsymbol{z}_0 = \boldsymbol{z}_0^\dagger\hat{V}_z\Sigma_z^2\hat{V}_z^\dagger\boldsymbol{z}_0, \tag{47}$$

where $\hat{U}_z\Sigma_z\hat{V}_z^\dagger$ is the SVD of $C\Phi_f P_0^{1/2}$. Each column $\hat{\boldsymbol{v}}_{zi}$ of the unitary matrix $\hat{V}_z$ corresponds to a normalized initial state $\boldsymbol{z}_0$. Setting $\boldsymbol{z}_0 = \hat{\boldsymbol{v}}_{zi}$ leads to a final state with an output $\boldsymbol{y}_f = \hat{\boldsymbol{u}}_i\varsigma_i$ that is aligned with the i'th largest semimajor axis of the final output covariance matrix $P_{y,f}$ ellipsoid, $\hat{\boldsymbol{u}}_i$. The corresponding output norm given by the i'th singular value in Σ_z, i.e., $\|\boldsymbol{y}_f\| = \varsigma_i$, is the length of the corresponding semimajor axis. Consequently, the maximum final output norm is the first singular value $\sigma_f = \varsigma_{z1}$, corresponding to $\boldsymbol{z}_0 = \hat{\boldsymbol{v}}_{z,1}$ and the initial state $\mathbf{x}_0 = P_0^{1/2}\hat{\boldsymbol{v}}_{z,1}$.

The maximum final output norm σ_f can also be evaluated from covariance propagation: the final output covariance matrix is $P_{y,f} = CP_fC^\dagger = C\Phi_f P_0\Phi_f^\dagger C = \hat{U}_z\Sigma_z^2\hat{U}_z^\dagger$ and its largest singular value is thus also $\sigma_f = \varsigma_{z1}$. However, covariance propagation does not provide information about the initial state $\boldsymbol{x}_0$ that leads to this maximum final output norm.

8.2 *LTI Systems with Impulsive Inputs*

This section focuses on LTI systems with a known number n of impulsive disturbances $\boldsymbol{w}_i$ with covariance matrices Q_i, taking place at $t = t_{w,i}$, where $1 \leq i \leq n$. For such systems, the framework defined above is applied by writing the final output as

$$\boldsymbol{y}_f = C\Phi_f\boldsymbol{x}_0 + \sum_{i=1}^{n} C\Phi_{w,i}\Gamma\boldsymbol{w}_i = C\tilde{\Phi}_f\tilde{\boldsymbol{x}}_0 = C\tilde{\Phi}_f\tilde{P}_0^{1/2}\tilde{\boldsymbol{z}}_0, \tag{48}$$

where $\Phi_{w,i} = \exp[A(t_f - t_{w,i})]$ and $\tilde{\Phi}_f = [\Phi_f, \Phi_{w,1}, \dots, \Phi_{w,n}]$. The initial augmented covariance matrix is

$$\tilde{P}_0 = \begin{bmatrix} P_0 & & & \\ & P_{w,1} & & \\ & & \ddots & \\ & & & P_{w,n} \end{bmatrix}, \tag{49}$$

where $P_{w,i} = \Gamma Q_i\Gamma^\dagger$ and $\tilde{P}_0^{1/2}$ is identified using SVD as before. The initial augmented likelihood state is $\tilde{\boldsymbol{z}}_0$, and the augmented initial state is $\tilde{\boldsymbol{x}}_0 = [\boldsymbol{x}_0^\dagger, \boldsymbol{w}_1^\dagger\Gamma^\dagger, \dots, \boldsymbol{w}_n^\dagger\Gamma^\dagger]^\dagger = \tilde{P}_0^{1/2}\tilde{\boldsymbol{z}}_0$.

Using the procedure from Sec. 8.1, the value of σ_f, i.e., the maximum output norm of $\|\boldsymbol{y}_f\|$ subject to $\|\tilde{\boldsymbol{z}}_0\| = 1$, is the first singular value of $C\tilde{\Phi}_f\tilde{P}_0^{1/2}$. The vector $\tilde{\boldsymbol{z}}_0$, given by the first right singular vector of $C\tilde{\Phi}_f\tilde{P}_0^{1/2}$, is the distribution of both initial uncertainties and impulsive disturbances that leads to $\|\boldsymbol{y}_f\| = \sigma_f$.

9 Appendix C: LTI System Output Norm Sensitivity

The initial covariance matrix can be decomposed in the same way as the disturbance covariance matrices $P_{w,i}$ in Sec. 8.2, by defining the block diagonal matrix

$$Q_0 = \mathrm{diag}(\sigma^2_{\delta\boldsymbol{\rho},\mathrm{sci}}I, \sigma^2_{\delta\boldsymbol{r},\mathrm{sci}}I, \sigma^2_{\delta\dot{\boldsymbol{\rho}},\mathrm{sci}}I, \sigma^2_{\delta\dot{\boldsymbol{r}},\mathrm{sci}}I, \sigma^2_{\delta\dot{\boldsymbol{s}},\mathrm{TCM}}I, \sigma^2_{\delta\dot{\boldsymbol{r}},\mathrm{TCM}}I, \sigma^2_{\delta\dot{\boldsymbol{s}},\mathrm{ret}}I), \tag{50}$$

such that $P_0 = \Gamma_0 Q_0 \Gamma_0^\dagger$, where Γ_0 is the corresponding matrix of coefficients that establish how the input sources of uncertainty are correlated to form P_0. Similarly, the full augmented initial covariance matrix is expressed as $\tilde{P}_0 = \tilde{\Gamma}_0\tilde{Q}_0\tilde{\Gamma}_0^\dagger$. Here, $\tilde{Q}_0$ is a diagonal matrix with elements that are the variances of the initial state and impulsive disturbances, and $\tilde{\Gamma}_0$ is the corresponding augmented coefficient matrix. The number $\tilde{n}$ of elements $\tilde{q}^2_{0i}$ in $\tilde{Q}_0$ and columns $\boldsymbol{\gamma}_{0,i}$ in $\tilde{\Gamma}_0$ is the sum of the number of impulsive disturbances n and the number of terms in Q_0, defined in Eq. (50).

Using this notation, it can be shown that the worst-case final relative position error σ_f for unity norm $\tilde{z}_0$ is the RSS of the contributions $\sigma_{f,i}$ from each of the $\tilde{n}$ sources of uncertainty in the system:

$$\sigma_f^2 = \sum_{i=1}^{\tilde{n}} \sigma^2_{f,i}, \tag{51}$$

where $\sigma_{f,i} = \boldsymbol{u}^\dagger_{y1} C\tilde{\Phi}_f\tilde{\boldsymbol{\gamma}}_{0,i}\tilde{q}_{0,i}$ and $\boldsymbol{u}_{y1}$ is the first singular vector of $\tilde{P}_{y,f} = C\tilde{\Phi}_f\tilde{P}_0\tilde{\Phi}_f^\dagger C^\dagger$. Normalizing leads to $\sum_{i=1}^{\tilde{n}} (\sigma_{f,i}/\sigma_f)^2 = 1$.

Similarly, the normalized sensitivity of σ_f to each term $\tilde{q}_{0,i}$ is given by the square of the corresponding normalized contribution:

$$\sigma'_{f,i} = \left(\frac{\tilde{q}_{0,i}}{\sigma_f}\right)\frac{\partial\sigma_f}{\partial\tilde{q}_{0,i}} = \left(\frac{\sigma_{f_i}}{\sigma_f}\right)^2. \tag{52}$$

As above, $\sum_{i=1}^{\tilde{n}} \sigma'_{f,i} = 1$ holds. The interpretation of this equation is that, if each term $\tilde{q}_{0,i}$ changes by a small amount $\partial\tilde{q}_{0,i}$ and becomes $\tilde{q}_{0,i} + \partial\tilde{q}_{0,i}$, then σ_f becomes $\sigma_f + \partial\sigma_f$, where

$$\frac{\partial\sigma_f}{\sigma_f} \approx \sum_{i=1}^{\tilde{n}}\left(\sigma_{f,i}{}'\frac{\partial\tilde{q}_{0,i}}{\tilde{q}_{0,i}}\right). \tag{53}$$

Acknowledgments

The research was carried out at the Jet Propulsion Laboratory, California Institute of Technology, under a contract with the National Aeronautics and Space Administration (80NM0018D0004) © 2020. All rights reserved. California Institute of Technology. Government sponsorship acknowledged.

References

1. S. Seager et al., “Imaging and spectra of exoplanets orbiting our nearest sun-like star neighbors with a starshade in the 2020s,” White Paper submitted to National Academy of Sciences, 2018, http://surveygizmoresponseuploads.s3.amazonaws.com/fileuploads/15647/4139225/235-0248419ac1193b0ada9e5ea5b64da7a1_SeagerSara.pdf.
2. M. Levine and R. Soummer, “Overview of technologies for direct optical imaging of exoplanets,” ASTRO2010 Community White Paper, 2009, http://authors.library.caltech.edu/57854/1/Levine_Visible%20Planet%20Imaging_TEC_EOS.pdf.

3. W. Cash et al., “External occulters for direct observation of exoplanets: an overview,” *Proc. SPIE* **6687**, 668712 (2007).
4. N. J. Kasdin et al., “Imaging extrasolar planets via formation flying with an external occulter,” *Adv. Astron. Sci.* **132**, 115–127 (2008).
5. M. Kochte et al., “External occulter operations requirements,” in *AIAA Space OPS Conf.* (2004).
6. W. Cash and New Worlds Team, “The new worlds observer: the astrophysics strategic mission,” *EPJ Web Conf.* **16**, 07004 (2011).
7. N. J. Kasdin et al., “Occulter design for THEIA,” *Proc. SPIE* **7440**, 744005 (2009).
8. S. Seager et al., “Exo-S: starshade probe-class exoplanet direct imaging mission concept, Final report,” 2015, http://exep.jpl.nasa.gov/stdt/Exo-S_Starshade_Probe_Class_Final_Report_150312_URS250118.pdf.
9. S. Seager, “Starshade Rendezvous probe study final report,” 2019, https://smd-prod.s3.amazonaws.com/science-red/s3fs-public/atoms/files/Starshade2.pdf.
10. B. S. Gaudi et al., “The Habitable exoplanet observatory,” *Proc. SPIE* **10698**, 600–604 (2018).
11. Astronomy Physics and Space Technology Directorate at the Jet Propulsion Laboratory, “HabEX final report,” 2019, https://www.jpl.nasa.gov/habex/pdf/HabEx-Final-Report-Public-Release.pdf.
12. T. L. B. Flinois et al., “Starshade formation flying II: formation control,” *J. Astron. Telesc. Instrum. Syst.* **6**(2), 029001 (2020).
13. J. Leitner, “Formation flying system design for a planet-finding telescope-occulter system,” *Proc. SPIE* **6687**, 66871D (2007).
14. D. P. Scharf et al., “Precision formation flying at megameter separations for exoplanet characterization,” *Acta Astron.* **123**, 420–434 (2016).
15. M. Bottom et al., “Starshade formation flying I: optical sensing,” *J. Astron. Telesc. Instrum. Syst.* **6**(1), 015003 (2020).
16. C. M. A. Deccia et al., “Surfing the L2 gradient with the starshade in search of extraterrestrial life,” in *AIAA/AAS Astrodyn. Spec. Conf.*, pp. 1–9 (2016).
17. C. M. A. Deccia, “Analysis of the Sun-Earth Lagrangian environment for the New Worlds Observer (NWO),” Master thesis, Delft University of Technology (2017).
18. S. W. Benson, A. S. Lo, and T. M. Glassman, “Solar electric propulsion for the new worlds observer terrestrial exoplanet mission,” in *45th AIAA/ASME/SAE/ASEE Joint Propul. Conf.*, pp. 1–12 (2009).
19. W. Cash et al., “The new worlds observer: the astrophysics strategic mission concept study,” *Proc. SPIE* **7436**, 74360 (2009).
20. J. S. Snyder et al., “Additional mission applications for NASA’s 13.3-kW ion propulsion system,” in *IEEE Aerosp. Conf. Proc.*, pp. 1–13 (2016).
21. C. C. Stark et al., “Maximized ExoEarth candidate yields for starshades,” *J. Astron. Telesc. Instrum. Syst.* **2**(4), 041204 (2016).
22. N. Rioux et al., “Engineering considerations applied to starshade repointing,” *Proc. SPIE* **9904**, 99043L (2016).
23. M. C. Noecker, “Alignment of a terrestrial planet finder starshade at 20-100 megameters,” *Proc. SPIE* **6693**, 669306 (2007).
24. D. K. Geller, “Linear covariance techniques for orbital rendezvous analysis and autonomous onboard mission planning,” *J. Guid. Control Dyn.* **29**(6), 1404–1414 (2006).
25. N. B. Stastny and D. K. Geller, “Autonomous optical navigation at Jupiter: a linear covariance analysis,” *J. Spacecr. Rockets* **45**(2), 290–298 (2008).
26. N. B. Stastny, R. A. Bettinger, and F. R. Chavez, “LinCov analysis of an automated celestial inertial navigate approach for GEO satellites,” in *AIAA/AAS Astrodyn. Spec. Conf.*, pp. 1–8 (2008).
27. D. K. Geller and D. P. Christensen, “Linear covariance analysis for powered lunar descent and landing,” *J. Spacecr. Rockets* **46**(6), 1231–1248 (2009).
28. J. W. Jang et al., “Linear covariance analysis for a lunar lander,” in *AIAA Guidance, Navig. and Control Conf.*, pp. 1–15 (2017).
29. M. B. Rose and D. K. Geller, “Linear covariance techniques for powered ascent,” in *AIAA Guidance, Navig. and Control Conf.* (2010).

30. D. K. Geller, “Analysis of the relative attitude estimation and control problem for satellite inspection and orbital rendezvous,” *J. Astron. Sci.* **55**(2), 195–214 (2007).
31. B. Gong, D. K. Geller, and J. Luo, “Initial relative orbit determination analytical covariance and performance analysis for proximity operations,” *J. Spacecr. Rockets* **53**(5), 822–835 (2016).
32. T. L. B. Flinois et al., “Efficient starshade retargeting architecture using chemical propulsion,” in *AAS/AIAA Astrodyn. Spec. Conf.*, AAS, pp. 20–421 (2020).
33. https://www.rocket.com/sites/default/files/documents/Capabilities/PDFs/Bipropellant%20Data%20Sheets.pdf (2020).
34. https://aerospace.honeywell.com/content/dam/aero/en-us/documents/learn/products/sensors/brochures/InertialNavigationSensors_bro.pdf (2020).
35. https://www.leonardocompany.com/documents/20142/3150068/Copia_di_A_STR_Autonomous_Star_Trackers_LQ_mm07786_.pdf?t=1538987562062 (2020).
36. R. J. Luquette and R. M. Sanner, “Linear state-space representation of the dynamics of relative motion, based on restricted three body dynamics,” in *AIAA Guidance, Navig. and Control Conf.*, p. 4783 (2004).
37. https://montepy.jpl.nasa.gov/static/document/brochure.pdf.
38. T. Carter and M. Humi, “Fuel-optimal rendezvous near a point in general keplerian orbit,” *J. Guidandce Control Dyn.* **10**(6), 567–573 (1987).
39. A. Farres, C. Webster, and D. Folta, “High fidelity modeling of SRP and its effect on the relative motion of starshade and WFIRST,” in *Space Flight Mech. Meeting*, pp. 1–15 (2018).
40. A. Farres, D. Folta, and C. Webster, “Using spherical harmonics to model solar radiation pressure accelerations,” *Adv. Astron. Sci.* **162**, 3365–3383 (2018).
41. E. Kolemen and N. J. Kasdin, “Optimization of an occulter-based extrasolar-planet-imaging mission,” *J. Guidance Control Dyn.* **35**(1), 172–185 (2012).
42. G. J. Soto et al., “Optimal starshade observation scheduling,” *Proc. SPIE* **10698**, 106984M (2018).
43. G. J. Soto et al., “Parameterizing the search space of starshade fuel costs for optimal observation schedules,” *J. Guidance Control Dyn.* **42**(12), 2671–2676 (2019).
44. P. J. Schmid, “Nonmodal stability theory,” *Annu. Rev. Fluid Mech.* **39**, 129–162 (2007).
45. S. R. Ploen, “Matlab covariance analysis tool (MCAT),” in *JPL Eng. Memorandum 343H-07* (2007).
46. C. Grubin, “Generalized two-impulse scheme for reorienting a spin stabilized vehicle,” *Prog. Astron. Rocketry, ARS, Guidance Control* **8**, 649–668 (1962).

Biographies of the authors are not available.